A methodological framework to study the behavior and kinetic influence of V, Mn, Co, Ni, Cu, Zn, As, Se and Mo during pyrite formation via the polysulfide pathway at ambient temperature

C. Baya, Pierre Le Pape, B. Baptiste, N. Menguy, L. Delbes, M. Morand, M. Rouelle, E. Aubry, G. Ona-Nguema, V. Noël, et al.

A methodological framework to study the behavior and kinetic influence of V, Mn, Co, Ni, Cu, Zn, As, Se and Mo during pyrite formation *via* the polysulfide pathway at ambient temperature

Baya C.[1], Le Pape P.[1*], Baptiste B.[1], Menguy N.[1], Delbes L.[1], Morand M.[1], Rouelle M.[2], Aubry E.[2], Ona-Nguema G.[1], Noël V.[3], Juillot F.[1], Morin G.[1]

[1] Institut de Minéralogie, de Physique des Matériaux et de Cosmochimie (IMPMC), UMR 7590 CNRS – Sorbonne Université – IRD – MNHN, case 115, 4 place Jussieu, 75252 Paris Cedex 5, France.

[2] Milieux Environnementaux, Transferts et Interactions dans les hydrosystèmes et les Sols (METIS), UMR 7619, Sorbonne Université – CNRS – EPHE, 4 place Jussieu, 75252 Paris Cedex 05, France.

[3]Stanford Synchrotron Radiation Lightsource, SLAC National Accelerator Laboratory, 2575 Sand Hill Road, MS 69, Menlo Park, CA 94025, USA

Chemical Geology

[*]corresponding author: pierre.le_pape@sorbonne-universite.fr

Abstract

Pyritization links the biogeochemical cycles of Fe, S and C to those of trace elements (TE) such as As, Ni, Cu, Co, Mn, Zn, Se and Mo in reducing environments. The scavenging modes of such impurities in pyrite are parameters of importance for evaluating to which extent pyrite can immobilize TE under diverse (sub)surface conditions. Furthermore, determining the fate of TE during pyritization is a prerequisite to determine the ability of pyrite to record the chemical signature of surrounding waters at the time of precipitation. Here, we provide a methodological framework to study the incorporation of TE during a reaction sequence leading to pyrite formation *via* the polysulfide pathway. Laboratory syntheses were conducted by reacting a FeS precursor with elemental sulfur – both readily obtained by reducing $FeCl_3$ with Na_2S in solution under strict anoxia – at ambient temperature and in the presence of aqueous V, Mn, Co, Ni, Cu, Zn, As, Se and Mo in a TE/Fe molar ratio of 0.5 mol%. Within this simplified framework, experiments aimed at reproducing the early formation of pyrite in water column aggregates/bottom sediments before the late diagenetic aging phases. Solids and liquids were sampled over time during the reaction sequence leading to pyrite formation, up to 3100 h, and were analyzed by ICP-OES, XRD, XRF and STEM-EDXS to obtain information on (1) the kinetics of pyrite formation and (2) the extent of TE incorporation in the solid phase, during and after the complete conversion of FeS to FeS_2. Pyrite formation kinetic is observed to be strongly influenced by the identity of the added TE, with the delay before nucleation decreasing in the order Ni >> Mn, Co > Cu, Zn, Se > Control, V >> As, Mo. During the full reaction sequence, *i.e.* FeS plus S(0) conversion to FeS_2, Mn remains in the liquid phase, Ni, Co, V, Cu, and Se quickly precipitate and remain sequestrated overtime, Zn and Mo precipitate and are further released into solution, and As is partially incorporated in the solid. Elemental mapping at the microscale using STEM-EDXS show that, except for Mn, the TE associated to the solids are present in pyrite. Moreover, while TE are homogeneously distributed at the particle scale for Co, Cu, Zn, As, and Se, Ni-pyrite exhibited an enriched core. The solid-liquid partition coefficients of each TE during our pyritization experiments in our simplified model system are calculated and ranks as follows: Cu ≥ Ni ≥ Co > Se > V > Mo >> As > Zn >> Mn. These partitions are discussed in the light of values reported in the literature from natural settings. The important differences observed exemplify the complexity to predict TE pyrite-water partition in sedimentary environments, in particular when considering additional multifactorial processes such as the local biogeochemistry of micro-environments, as well as the partial sequestration of TE by non-sulfide minerals such as authigenic clays and carbonates.

Keywords

Sedimentary pyrite, trace elements, paleoenvironments, early diagenesis, precipitation rate, kinetics

Graphical abstract

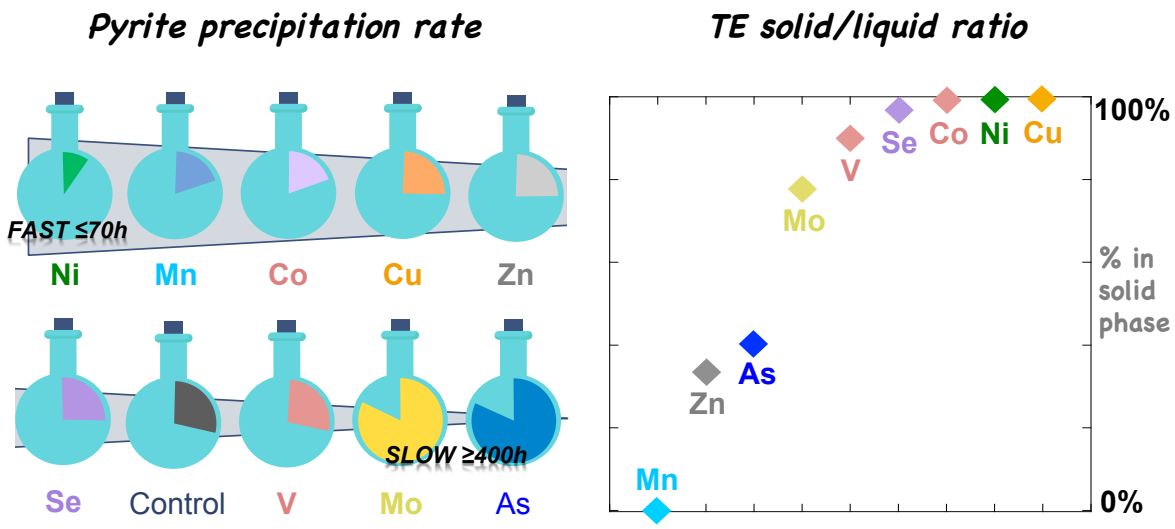

1. Introduction

Authigenic pyrite is widely observed in Earth's surface environments, both in marine and continental settings. As the more thermodynamically stable iron sulfide mineral (Berner, 1967; Rickard and Luther, 2007), it presents an exceptional capacity to persist in sedimentary environments (*e.g.* Wacey *et al.*, 2011), making it a major geochemical proxy of depositional conditions (Raiswell and Canfield, 1998; Rouxel *et al.*, 2005; Marin-Carbonne *et al.*, 2014). Several studies have shown that numerous metallic and metalloid ions have strong affinities for sedimentary pyrite (FeS_2) (Dill and Kemper, 1990; Huerta-Diaz *et al.*, 1998; Large *et al.*, 2014; Gregory *et al.*, 2015a; Noël *et al.*, 2015; Le Pape *et al.*, 2017; Morin *et al.*, 2017; Baya *et al.*, 2021). For instance, nickel (Ni), arsenic (As) and selenium (Se) ions are able to sorb at the pyrite surface or to substitute for iron (Fe) and/or sulfur (S) ions in the pyrite structure (Raiswell and Plant, 1980; Jean and Bancroft, 1986; Dill and Kemper, 1990; Morse and Arakaki, 1993; Savage *et al.*, 2000; Farquhar *et al.*, 2002; Bostick and Fendorf, 2003; Scholz and Neumann, 2007; Deditius *et al.*, 2008; Diener and Neumann, 2011; Diener *et al.*, 2012; Gregory *et al.*, 2015a; Le Pape *et al.*, 2017; Manceau *et al.*, 2020; Baya *et al.*, 2021). In addition, traces of other metallic and metalloid elements such as vanadium (V), manganese (Mn), cobalt (Co), copper (Cu), zinc (Zn) and molybdenum (Mo) are observed in pyrite (Large *et al.*, 2009, 2014; Gregory *et al.*, 2015a; Parnell *et al.*, 2018; Mukherjee *et al.*, 2019). Thus, pyrite constitutes both a sink and a source for these elements (Huerta-Diaz and Morse, 1992; Zhang *et al.*, 2002; Thomas *et al.*, 2011; Large *et al.*, 2012), some of which (such as As and Ni) being particularly harmful to humans and ecosystems (*e.g.* Denkhaus and Salnikow, 2002; Ratnaike, 2003). Since pyrite is abundant in surface environments, it is essential to understand the mechanisms that control the scavenging of minor and trace elements by this mineral that can impact their biogeochemical cycling.

The chemical composition of sedimentary pyrite has been proposed as a geochemical indicator of past geological and climatic events, notably because this mineral reflects trace element signatures of oceanic paleo-environments (Large *et al.*, 2014; Gregory *et al.*, 2015; Mukherjee and Large, 2020). For instance, recent works from Mukherjee *et al.* (2019) have concluded that the concentrations of Se and Mo in pyrite can be used as redox-sensitive markers of oxygenation levels in ancient oceans and atmosphere. Indeed, the abundance and distribution of trace elements in sedimentary pyrites is documented from LA-ICPMS and EPMA analyses (Large *et al.*, 2014, 2017; Marin-Carbonne *et al.*, 2014; Gregory *et al.*, 2015b; Li *et al.*, 2017; Mukherjee and Large, 2020; Chen and Campbell, 2021; Wang et al.

106 2021) and is used to estimate the chemical composition of ancient oceanic water-bodies
107 and/or to discuss the phasing of different diagenetic steps. For instance, Large *et al.* (2014)
108 have estimated ancient ocean chemistry on the basis of a positive log relationship observed
109 between trace element compositions of mean modern oceanic water and of actively forming
110 pyrite in the Cariaco Basin on the Venezuela shelf (Large *et al.*, 2014, 2017). Other studies
111 have focused on the content of some trace elements in pyrite nodules, possibly presenting a
112 complex diagenetic history, and have related the chemical composition of the core of the
113 pyrite nodules with water geochemistry at the time of deposition (Marin-Carbonne *et al.*,
114 2014; Li *et al.*, 2017; Chen and Campbell, 2021). Although these approaches are helpful for
115 assessing past ocean trace element compositions, further understanding of trace element
116 speciation and solid/liquid partitioning during pyrite precipitation at low temperature could
117 contribute to refine these geochemical reconstructions.
118 For instance, recent works have shown that the presence of metal and metalloid
119 impurities in the synthesis medium can affect pyrite formation kinetic, which in turn can
120 influence the solid/solution partition coefficient for these elements. For instance, Morin *et al.*
121 (2017) and Baya *et al.* (2021) have demonstrated that minor to trace concentration levels of
122 Ni in solution accelerate pyrite nucleation at ambient temperature, whereas, Le Pape *et al.*
123 (2017) and Baya *et al.* (2021) have shown that As(III) delays pyrite formation at room
124 temperature. Extended X-ray Absorption Fine Structure (EXAFS) analyses performed in these
125 studies showed that rapid incorporation of Ni into the first stages of pyrite nucleation leads to
126 complete sequestration of Ni into the pyrite structure at the Fe site, while a significant
127 proportion of As remains sorbed or segregated at the surface of pyrite particles, in addition to
128 As incorporated at the S and Fe sites. Such distinct behaviors of these trace elements may
129 influence their solid-liquid partition coefficients during pyritization processes in natural
130 systems and thus deserve to be further studied. A major limitation for determining such
131 partition coefficients, however, relies on the complexity of pyrite nucleation and growth
132 processes at low temperature, for which multiple lines of explanation have been proposed,
133 especially regarding the importance of colloidal/aqueous FeS and polysulfide precursors of
134 pyrite (Berner, 1964; Rickard, 1975; Berner, 1984; Luther, 1991; Wilkin and Barnes, 1996,
135 1997; Benning *et al.*, 2000; Butler and Rickard, 2000; Rickard and Luther, 2007; Matamoros-
136 Veloza *et al.*, 2018a; Baya *et al.*, 2021). Recently, Baya *et al.* (2021) have confirmed the
137 nanosize and mixed Fe(II)/(III) valence form of the main FeS_{nano} precursor of pyrite
138 (Wolthers *et al.*, 2003; Matamoros-Veloza *et al.*, 2018a, b). The same authors propose that the

interaction of Ni and As with this precursor as well as with the pyrite nuclei and polysulfides influence pyrite formation kinetic and would partly control the affinity of these trace elements for this mineral. Therefore, investigating the influence of a larger panel of elemental impurities on pyrite formation kinetic under controlled laboratory conditions, approaching early diagenetic environments, could help to better understand the mechanisms that control the solid-liquid partition of trace elements in pyrite. To this regard, trace elements such as V, Mn, Co, Ni, Cu, Zn, As, Se and Mo are frequently observed in sedimentary pyrite, in which they occur within the thousand ppm wt. range, and locally reach a few wt% (Large *et al.*, 2009; Gregory *et al.*, 2015a; Noël *et al.,* 2015).

Based on these considerations, the main objective of the present study is to provide an experimental framework to determine to which extent a set of metallic and metalloid trace elements introduced as dissolved species interfere in the pyrite formation sequence at ambient temperature and whether they have a measurable influence on pyrite formation kinetic. Additionally, we aim at drawing hypotheses on their mode of association with the FeS precursors and pyrite on the basis of STEM-EDXS mapping data and of available literature. For this purpose, we have performed pyrite syntheses at ambient temperature *via* the polysulfide pathway, *i.e.* by reacting Fe(III) with H_2S to immediately yield FeS plus S(0) that ultimately converts into FeS_2 accompanied by aqueous Fe^{2+} (Noël, 2014; Noël *et al.*, 2015; Le Pape *et al.*, 2017; Morin *et al.*, 2017; Sheng *et al*. 2019; Baya *et al.*, 2021). This pyrite synthesis route leads to $Fe_T = Fe_{Py} + Fe^{2+}$ and yields a ratio $Fe_{py}/Fe_{HR(=FeT)} = 0.5$, where FeT is total Fe, and FePy Fe in pyrite, which is relevant to ferruginous early diagenetic conditions as described by Poulton and Canfield (2011). The synthesis experiments were conducted in the presence of each of the selected metal and metalloid ions in the starting solution. Thanks to detailed time-course analyses of solids and liquids, we were able to determine that pyrite formation was differently affected by each of the trace elements, with observed kinetics depending on the added element. We discuss the modes and rates of incorporation of the studied trace elements during early pyrite precipitation and compare the solid-liquid partition obtained with values available in the literature.

2. Materials and Methods

2.1. Pyrite syntheses in the presence of trace elements

Ten distinct batch pyrite syntheses were carried out at room temperature (25 ± 3 °C) within an anoxic glove box: nine batches with addition of either V(V), Mn(II), Co(II), Ni(II), Cu(II), Zn(II), As(III), Se(II) or Mo(VI) meant to form pyrite doped in the respective trace element, and a control synthesis referred to as "Fe-S", devoid of trace elements and meant to form pure pyrite. The synthesis protocol was adapted from previous studies by Morin *et al.* (2017), Le Pape *et al.* (2017), and Baya *et al.* (2021), as the initial synthesis solutions were added with a single trace element (TE) at a TE/Fe molar ratio of 0.5% (Table 1). Although being in the upper-end of natural ranges typically observed for the studied TEs in sedimentary pyrites (Gregory et al., 2015a), this value was chosen to maximize the expected kinetic effect of TE on pyrite formation.

Table 1. Proportions of the reactants used for the pyrite synthesis experiments conducted with various trace elements in 100mL anoxic glass vials with a total liquid volume of 50.16 mL.

Reactants	Stock solutions		Reaction vials (50 mL)	
	C (M)	*v* (mL)	*n* (mmol)	*c* (mM)
$FeCl_3.6H_2O$	0.625	6	3.75	75
Trace element salt*	0.1	0.19	0.019	0.38
O_2-free milli-Q water		38		
$Na_2S.9H_2O$	0.625	6	3.75	75

Notes: * Trace element salt for each synthesis experiments referred to as Fe-S, Fe-S:V, Fe-S:Mn, Fe-S:Co, Fe-S:Ni, Fe-S:Cu, Fe-S:Zn, Fe-S:As, Fe-S:Se and Fe-S:Mo was the following : none, $Na_3VO_4.xH_2O$, $MnCl_2.4H_2O$, $CoCl_2.6H_2O$, $NiCl_2.6H_2O$, $CuCl_2.2H_2O$, $ZnCl_2$, $NaAsO_2$, Na_2SeO_3 and $Na_2MoO_4.2H_2O$, respectively; *C*, *v* and *c* value for Fe-S:V were 0.14 $mol.L^{-1}$, 0.16 mL and 0.44 $mmol.L^{-1}$, respectively. More details on the salts used for the synthesis experiments are listed in the Table SI-2.

In this synthesis pathway (Wei and Osseo-Asare, 1997; Noël, 2014; Noël *et al.*, 2015; Le Pape *et al.*, 2017; Morin *et al.*, 2017), aqueous sulfide immediately reduces ferric iron and form nanosized iron monosulfide precursors "$FeS_{(cluster,nanoMck)}$" (Baya *et al.* 2021), together with S(0), polysulfides and aqueous Fe^{2+}. Briefly, this first step can be summarized by the following reaction, in which soluble Fe(III) reacts with aqueous H_2S to form iron monosulfide FeS and S(0):

$$Fe(OH)_2^+ + H_2S = ½\ FeS + ½\ S(0) + ½\ Fe^{2+} + 2\ H_2O \qquad \text{(Eq. 1)}$$

Subsequently, after a lag phase, $Fe_xS_{x(aq)}$ species, likely forming a continuum with the aggregated $FeS_{(cluster,nanoMck)}$ precursor in our high salinity system (8.7 $g.L^{-1}$, Table 1), react with polysulfides in solution and fully convert to pyrite, as detailed by Morin *et al.* (2017) and Baya *et al.* (2021). This second step can be written in a simplified way as the following net reaction:

$$½\ FeS + ½\ S(0) = ½\ FeS_2 \qquad \text{(Eq. 2)}$$

Thus, the final solid iron product is pure pyrite that coexists with aqueous Fe^{2+} at a $Fe_{py}/Fe_{HR(=FeT)}$ ratio of 0.51 (and 0.59 for the V-doped synthesis), which is relevant to ferruginous early diagenetic conditions (Poulton and Canfield, 2011).

In order to avoid any oxidation of the synthesis suspensions, the experiments were performed in a Jacomex™ glove box (< 2 ppm O_2) under a nitrogen atmosphere and using O_2-free milli-Q water, degassed by bubbling N_2 at 80°C during 45 min. Stock solutions of $Na_3VO_4.xH_2O$, $MnCl_2.4H_2O$, $CoCl_2.6H_2O$, $NiCl_2.6H_2O$, $CuCl_2.2H_2O$, $ZnCl_2$, $NaAsO_2$, Na_2SeO_3 or $Na_2MoO_4.2H_2O$ were prepared in the glove box and were magnetically stirred for 3 days before the experiments start. For the control synthesis (Fe-S), 6 mL of the $FeCl_3$ stock solution was mixed with 38 mL of O_2-free milli-Q water under stirring. For the trace elements-doped syntheses, appropriate volumes (v) of stock solutions of $Na_3VO_4.xH_2O$, $MnCl_2.4H_2O$, $CoCl_2.6H_2O$, $NiCl_2.6H_2O$, $CuCl_2.2H_2O$, $ZnCl_2$, $NaAsO_2$, Na_2SeO_3 or $Na_2MoO_4.2H_2O$ were mixed with the initial 6 mL of $FeCl_3$. Afterwards, 38 mL of water was added to the mixture. Then, 6 mL of Na_2S solution were added, reaching a final volume of 50 mL (V_{total}) in the glass vials (Table 1).

The syntheses suspensions were kept under constant stirring during 3100 hours (≈ 129 days) using magnetic stir bars placed in the glass vials before sealing them with butyl rubber stoppers. Over the course of every experiment (TE-containing plus control), solids and solutions were sampled within the anoxic glove box at specific time-steps (*i.e.* 0.5, 70, 118, 170, 235, 330, 409 and 3100 hours.) and pH measurements were carried on at each sample collection. For more detailed kinetic of pyrite formation in the presence of Ni and As, respectively at the beginning and at the end of the investigated time-range, please refer to Morin et al. (2017) and Baya *et al.* (2021). As decribed in Baya et al. (2021), when pyrite formation occurs, the matt black colour of the suspension turns to anthracite grey, which has helped to determine the timesteps for sample collection. The samples were referred to as Fe-

S_*N*h, for the control experiment and Fe-S:TE_*N*h, for the nine batch synthesis experiments, where TE stands for the corresponding trace element and *N*h stands for the sampling time after start in hour units. At each sampling time, the solid phase was sampled by centrifuging 2.7 mL of the solution at 15,000 rpm during 3 to 5 minutes in the glove-box. Afterwards, the solids were washed twice with O_2-free milli-Q water and vacuum-dried in a desiccator within the glove-box (Le Pape *et al.*, 2017; Morin *et al.*, 2017). In the meantime, supernatants were filtered through 0.2 µm cellulose filters, diluted 100 times in HNO_3 solution (1%), and stored in anoxic vials within the glovebox for further elemental analyses.

2.2. Mineralogical and chemical analysis of the solid phases

For mineralogical analyses, a few tens of mg of solid was recovered by centrifugation at each sampling time, which was suitable for analysis with the focused X-Ray beam. Prior to data collection, the powder samples were mounted between two 50µm-thick layers of Kapton® Tape within the glove box to limit potential changes in the mineralogy due to redox reactions with air during the analysis. Powder X-Ray Diffraction (XRD) patterns of the solid samples were collected in Debye-Scherrer configuration using a Rigaku MM007HF Mo rotating anode source ($\lambda_{K\alpha1}$=0.709319 Å, $\lambda_{K\alpha2}$=0.713609 Å), operating at 50kV and 24mA, equipped with a Varimax focusing optics and a RAXIS4++ image plate detector installed at a distance of 205 mm of the sample. For each sample, XRD powder patterns were collected between 0° and 47° 2θ during 30 minutes to 2 hours at 20°C. The beam size was fixed to 80 µm. The step-size chosen for the numerical integration step was fixed to 0.01°. Data integration was performed with the Fit2D software (Hammersley, 2016).

The same samples were analyzed by X-Ray Fluorescence (XRF) using the Rigaku MM007HF Mo rotating anode equipped with Si-drift KETEK™ detector with an acquisition time of 30 minutes to 1 hour per sample. Emission spectra were calibrated in energy on the basis of the positions of Fe Kα and Fe Kβ emission lines. These measurements allowed us to determine the presence of S, V, Mn, Fe, Co, Ni, Cu, Zn, As, and Se in the solid samples over the course of the synthesis experiment.

Scanning Transmission Electron Microscopy (STEM) was performed at the IMPMC on the final 3100h samples from the Fe-S:Co, Fe-S:Zn, Fe-S:Se, Fe-S:Ni, Fe-S:As and Fe-S:Mo synthesis experiments using a JEOL 2100F microscope operating at 200kV with a field emission gun. Qualitative chemical mapping and local elemental compositions were obtained by energy dispersive X-ray spectroscopy (EDXS) using a JEOL detector to identify the added

elements in the pyrite particles. In addition, selected area diffraction (TEM-SAED) patterns were also collected with the same microscope, corresponding to data being reported in the supporting information section (Fig SI-13). The Fe-S:Cu sample was not analyzed because of EDXS interferences with the carbon-coated Cu-grid used as sample holder. The Fe-S:Mn was not selected for STEM-EDXS analysis due to low Mn concentrations calculated form chemical balance (Table SI-1), expected to be bellow the EDXS detection limit. The Fe-S:V sample could not be analyzed because of poor sample preparation.

2.3. Chemical analysis of the liquid phases

The diluted supernatants were analyzed by inductively-coupled plasma-optical emission spectrometry (ICP-OES) (AGILENT 5100 SVDV) on the ALIPP6 platform at Sorbonne University, to determine the concentrations of V, Mn, Fe, Co, Ni, Cu, Zn, As, Se and Mo, in each of the liquid samples collected over the course of the experiment. Ten blanks were submitted to the same treatment for method control. The detection limits of V, Mn, Fe, Co, Ni, Cu, Zn, As, Se and Mo were 0.5, 1.7, 12.6, 1.1, 1.2, 3.0, 10.8, 8.0, 10.0 and 3.0 ppb, respectively. Measurement accuracies were controlled using standard references of each element with concentrations of 0-4-8-16-32-50-100-200 and 400 ppb, plus using reference samples of known concentration. Typically, error on the measurements were <5% as measured repeatedly on a 8 ppm standard reference sample for each element studied, except for As and Se for which the error was <10%.

3. Results

3.1. Kinetic evolution of the solids mineralogy during the syntheses

The onset of pyrite formation was found to significantly differ as a function of the TE added in the starting solution (Figure 1), as revealed by powder XRD analyses of the solids collected over the course of the syntheses (Figure 2 and Figures SI-1 to SI-10). Pyrite was detected after 235 hours in the control experiment (Fe-S) and was fully formed after 330 h (Figure SI-1) as well as in the Fe-S:V experiment (Figure SI-8). In contrast, in agreement with previous studies (Morin *et al.*, 2017; Baya *et al.*, 2021), the presence of Ni dramatically accelerated the formation of pyrite that was fully formed at 70 hours (Figure 1 and SI-2). Mn in the initial solution lead to a moderate acceleration of pyrite formation, as pyrite was fully formed at 118 hours (Figure SI-3). Co also accelerated pyrite formation since the first pyrite grains were observed at 118 hours (Figure SI-4). Cu, Zn and Se appeared to induce a slight acceleration in pyrite formation, with first pyrite detection at 170h (Figure SI-5, Figure SI-6 and Figure SI-7, respectively). Finally, Mo and As significantly slowed down pyrite precipitation with respect to the control, since the first pyrite grains were detected at 3100 hours (Figure SI-9 and Figure SI-10, respectively). This observation indicates that pyrite nucleation occurred between 409 hours and 3100 hours in these two latter synthesis experiments. The delay effect of As is consistent with the previous study by Baya *et al.* (2021). Figure 1 summarizes these results from XRD analysis, showing that the various TE investigated distinctly impact the kinetics of pyrite formation in our experiments. Since the experiments were performed at the same time, in the same conditions and with similar TE/Fe molar ratio and within the same pH range (Figure SI-11), the observed formation rates can be considered as depending essentially on the identity of the added TE in the initial solution.

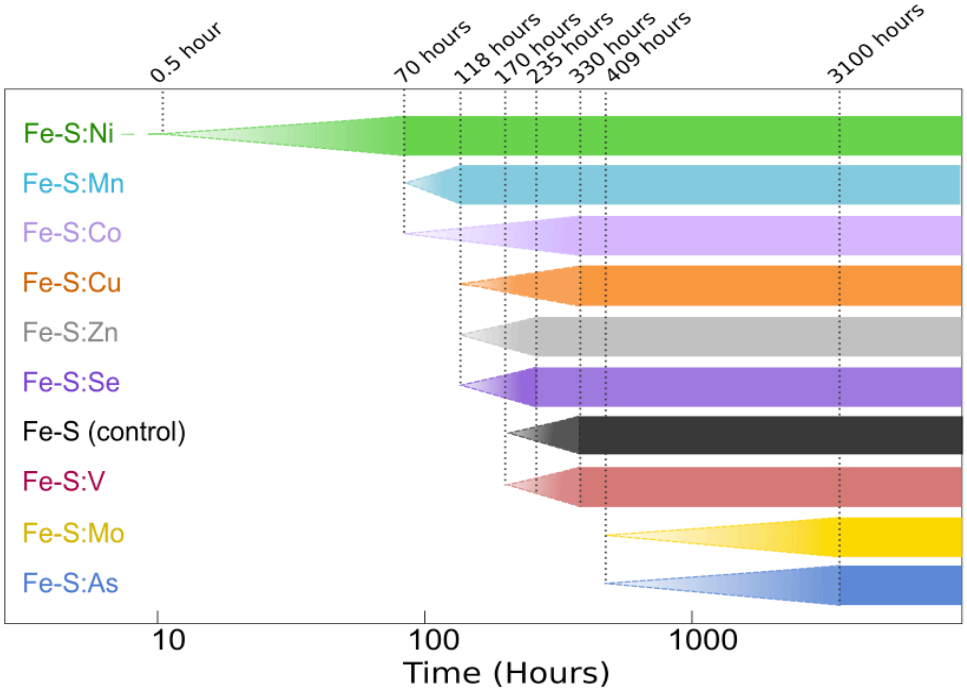

Figure 1. *Onset of pyrite formation as a function of the added trace element, as determined by XRD analysis (Figure 2, and Figure SI-1 to Figure SI-10). The elongated triangles represent the time-lapse between the last XRD pattern showing no pyrite and the first XRD pattern in which pyrite is the dominant iron-sulfide mineral. Thus, pyrite nucleation occurred between the tip and the base of the triangles for each experiment.*

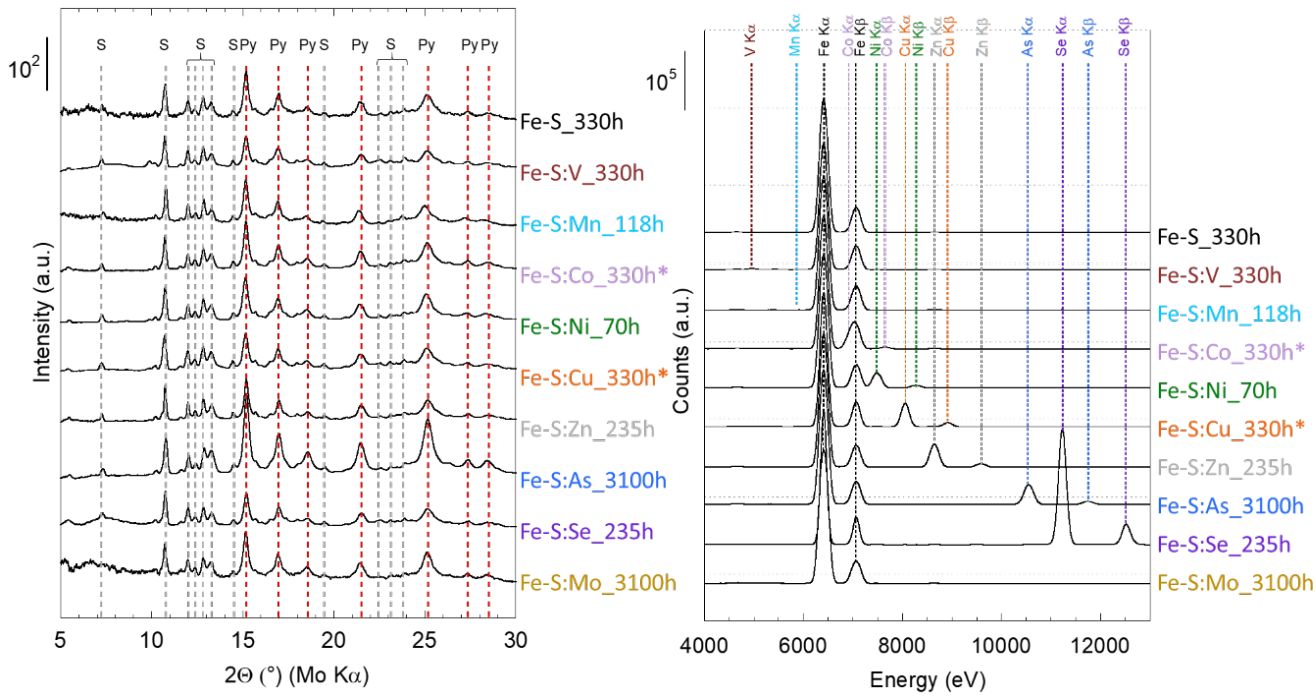

Figure 2. *Mineralogical and chemical composition of the solids at the onset of pyrite formation. Left: XRD patterns showing Py = Pyrite, S = zero-valent α-sulfur. Right: XRF spectra normalized to the Fe Kα emission line for the same samples. Notes: *The Fe-S:Co and Fe-S:Cu samples already displayed*

weaker pyrite peaks at 118 and 170 hours respectively (Figure 1; Figure SI-4 and Figure SI-5 respectively). Mo Kα and Kβ lines could not be observed using our Mo Kα X-ray source and Mo L lines were fully absorbed by air at such Mo concentration in the solid.

Figure 2 displays, for each synthesis experiment, the powder XRD pattern of the first time-step sample in which pyrite is the dominant iron-sulfide mineral phase. At these time-steps the FeS precursor was fully converted to pyrite, as shown by the complete time-course series of XRD patterns for each TE experiment (Figure SI-1 to Figure SI-10). In these series, complete conversion of FeS to pyrite is recognized by the absence of detectable FeS signal together with a pyrite pattern having reached its maximum intensity. Such a complete conversion of the FeS precursor into pyrite is consistent with previous syntheses experiments conducted using a similar protocol (Le Pape *et al.*, 2017; Morin *et al.*, 2017; Baya *et al.*, 2021). If Fe(III) and H_2S are initially introduced in strict equimolar conditions, only $FeS_{2(solid)}$ and $Fe^{2+}_{(aqueous)}$ will remain at the end of the experiment, while FeS and S(0) only stand as transient intermediates during the lag phase. If Fe and S are not initially in equimolar proportions, the final solid mix will include additional FeS or S(0), depending on the initial species in excess.
In the present study, residual elemental α-sulfur was observed in the final samples after the full pyrite synthesis sequence (Figure 2, Figure SI-1 to Figure SI-10), suggesting that the $FeCl_3$ and Na_2S reactants were not present in exact equimolar concentrations as expected from Table SI-1. This observation could indicate that a slight degassing of the H_2S solution might have occurred prior to the start of the syntheses (pH~5.5) and/or that the $Na_2S.9H_2O$ salt employed was more hydrated than expected. Either of these causes actually imply that starting H_2S concentrations were lower than expected, leading to less initial FeS production and thus to more elemental sulfur and aqueous Fe^{2+} remaining after full conversion of FeS to pyrite. However, this deviation from the ideal reaction stoichiometry did not affect the nature of the iron sulfide produced and was strictly similar for all experiments that were conducted at the same time using the same reactants.

3.2. Variations of total Fe and pH during the syntheses experiments

Chemical composition of the filtered suspensions collected during the synthesis experiments are reported in Table SI-1 and are plotted for pH and dissolved Fe in Figure SI-11 and Figure SI-12. The amount of Fe in the liquid fraction decreased from 3.75 mmol to around 1.9 mmol (1.87 to 1.98 mmol) at the last time-step (3100 h) for every experiment, which attested that pyrite was produced in similar amount whatever the trace element used

and that despite the initial inputs of Fe and S were not exactly equimolar. The time profiles are relatively similar and show that most of Fe precipitation occurred between 70 h and 409 h.

The pH values measured from 0.5 hours to 3100 hours show variations over time in the 5.8 to 3.8 range. At 0.5 h after Fe(III) and H_2S mixing, the initial pH ranged between 5.3 (control Fe-S, Fe-S:Mn, Fe-S:Co, and Fe-S:Zn experiments) and 5.6 (Fe-S:As). For all experiments, the pH was relatively stable during the lag phase before pyrite nucleation, slightly increasing in some experiments, especially to 5.8 in the Fe-S:Mo and Fe-S:As experiments, and decreasing for others, especially in the Fe-S:Mn experiment. Pyrite formation then coincided with a significant pH drop to reach final values within the 4.4. to 4.8 range. The lag phase pH value was the highest in the Fe-S:As and Fe-S:Mo experiments where pyrite formation was slowed down, which may have limited the H^+ production that is reported to accompany pyrite formation in this synthesis pathway (Baya *et al.*, 2021).

3.3. Solid/liquid partition of the trace elements

The results of ICP-OES analyses of the filtered supernatants and XRF analyses of the solids collected allowed us to estimate the distribution of trace elements between the liquid and solid phases over the course of the pyrite syntheses. XRF spectra for the complete series of samples are displayed in Figure SI-1 to Figure SI-10. Selected spectra reported in Figure 2 correspond to the first time-step at which the FeS precursor was fully converted to pyrite and thus yield direct information on the scavenging of the studied trace elements by the S(0) and FeS_2 mineral mixture. Manganese was non-detectable in the solids formed suggesting that its incorporation in the solid phase was negligible, if any (Figure 3). Molybdenum emission lines analysis was not achievable with our XRF setup because it uses incident Mo *K* radiation (Figure SI-9). Apart from these two latter ones every other element (Ni, Co, Cu, Zn, Se, V and As) was detected by XRF in the bulk solids. The variations observed in the intensity of trace element emission lines as a function of time (Figure SI-1 to Figure SI-10) may result from different trace element enrichments of the mineral phases constituting the solids, i.e., mostly FeS, followed by FeS_2 over time. In addition, possible heterogeneities in the samples may account for part of the observed variations, even if the XRF measurements were performed in the same conditions. Nevertheless, the presence of each trace element in pyrite, but Mn (and Mo) was attested by XRF spectra after full conversion of the FeS precursor into pyrite (Figure 2).

The aqueous concentrations of trace elements and Fe were monitored over time in the liquid phase (Figure 3, left), allowing us to derive the trace element contents in the solid phase, referred to as TEsolid (ppm wt.) (Figure 3, right). It represents the trace element concentration associated to the pyrite phase after the whole Fe pool in the solid has converted to pyrite (Figure 1 and Figure 2), as indicated by a colored region in Figure 3, right. With the exception of Mn and As, every added trace element was quickly sequestrated by the solid phase (Figure 3). Indeed, despite the slight acceleration of pyrite formation in the presence of Mn, this element remained mostly in solution from the beginning to the end of the synthesis. Conversely, As, which slows down pyrite formation (Figure 1) (Wolthers *et al.*, 2007; Baya *et al.*, 2021), partially associated with the solid phase (Le Pape *et al.*, 2017). All of the other trace elements investigated, i.e. V, Co, Ni, Cu, Co, Ni, Cu and Se, rapidly precipitated from solution and remained sequestered in the solid until and after complete conversion of FeS to FeS_2. Interestingly, Mo and Zn were further partially released over time during the pyritization stage, as well as V at a minor level (Figure 3).

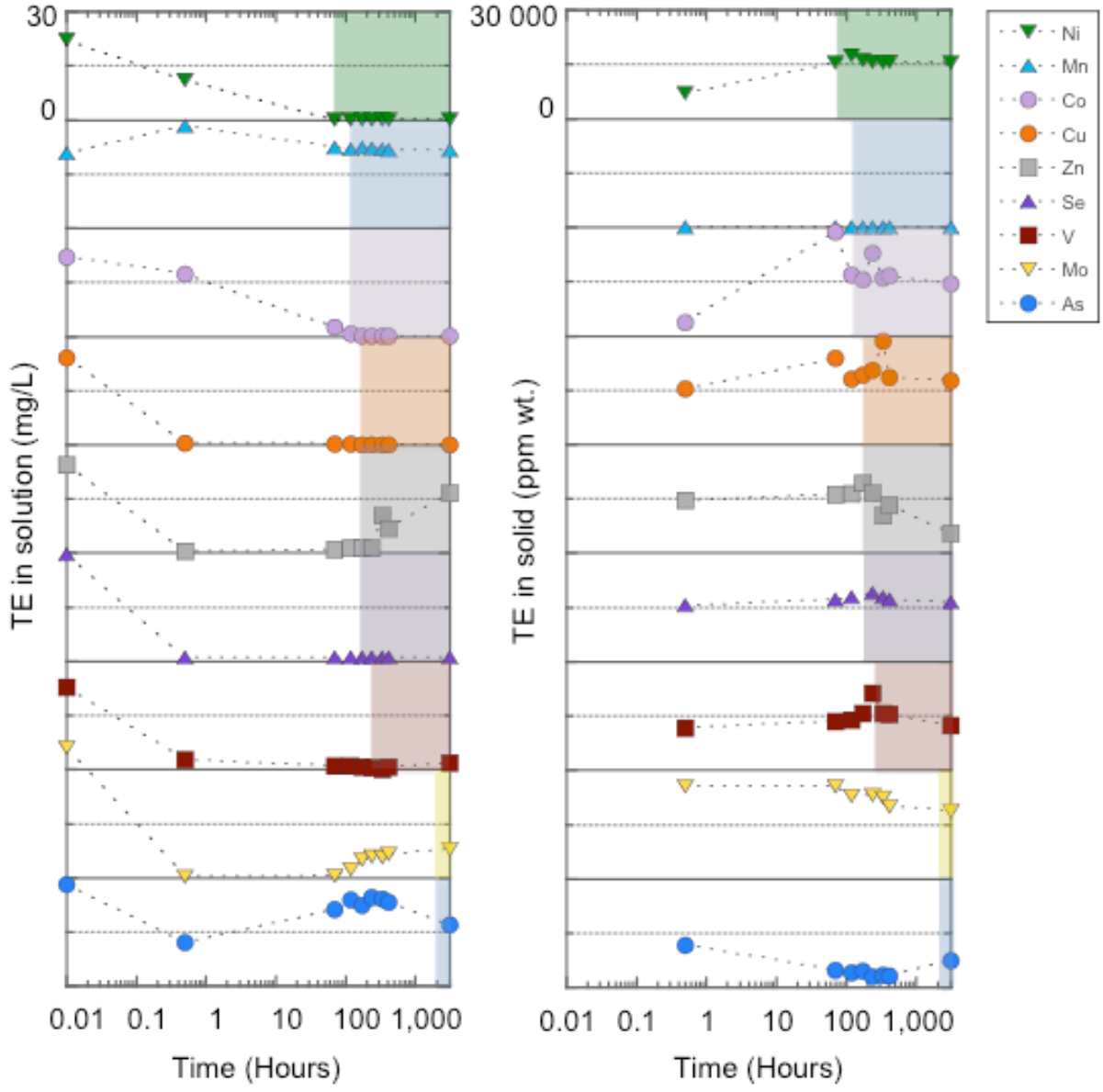

Figure 3. *Time-course evolution of the trace elements concentrations in the aqueous and solid phases. Left: aqueous concentrations of trace elements (ppm, i.e. mg.L^{-1}), on the same scale for every TE, as measured by ICP-OES, but the starting point that corresponds to the added TE. Right: TE/FeS_2 ratio (ppm wt.) in the solid phase calculated by difference between the initial and measured aqueous concentrations. The colored sections correspond to the onset of pyrite formation (Figure 1). Corresponding data are reported in Table SI-1.*

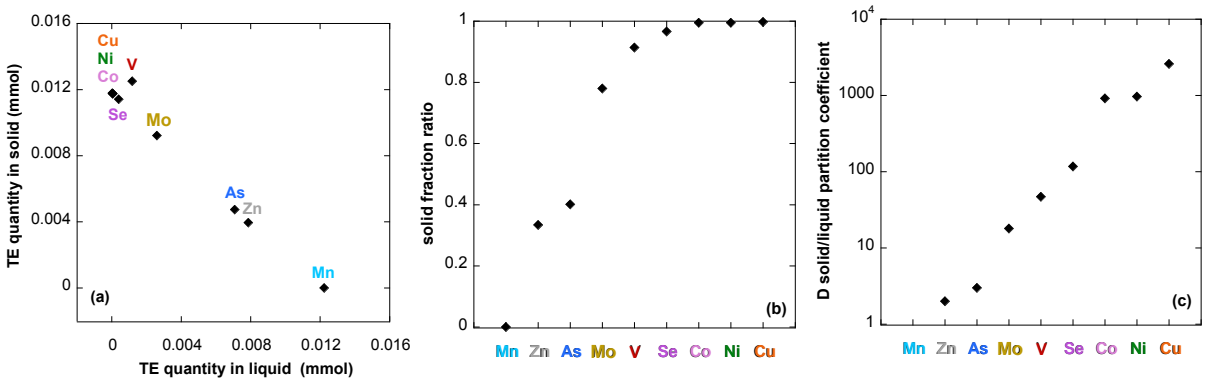

Figure 4. *Solid-liquid partition of the trace elements (TE) at the end of our pyrite syntheses (3100 h). (a) TE quantity (mmol) in the solid phase as a function of TE quantity (mmol) in the liquid phase (mmol). (b) solid fraction ratio = $TE_{solid}/(TE_{solid}+TE_{liquid})$ (mol/mol).(c) Solid-liquid partition coefficient, $D = TE_{solid}/Fe_{solid} / (TE_{liquid}/Fe_{liquid})$ as molar ratios, log scale.*

Finally, the partition coefficients between the solid and liquid phases (Figure 4) could be determined from the measured TE concentrations in the liquid phase at the end of the pyrite synthesis by difference from the initial amount of TE added in the synthesis medium (Figure 3). The results show that Cu, Ni and Co were fully (> 99%) sequestered by pyrite, followed by Se, V and Mo that were preferentially associated to pyrite (~80-90%), while As and Zn were preferentially retained in the aqueous phase (<40% in pyrite). As already shown by XRF data (Figure 2 and Figure SI-3), Mn was not associated with the solid and remained in the aqueous phase. Partition coefficients, referred to as *D*, determined according to McIntire *et al.* (1963) formalism, are also presented in Figure 4. Such coefficients are presented for the first time in the literature for the set of trace elements studied, in pyrite obtained at ambient temperature. The observed *D* values sort in the same trace element order as the other indexes presented in the same Figure 4 and fall within the 0 - 10^4 range.

3.4. Trace elements distribution at the nanoscale

STEM-EDXS analyses of the final samples from the Fe-S:Ni, Fe-S:Co, Fe-S:Zn, Fe-S:Se, Fe-S:Mo and Fe-S:As experiments bring information on the size and morphology of the pyrite after 3100 hours of synthesis as well as on the spatial distribution of trace elements at the nanoscale (Figure 5). The submicron pyrite grains were directly identified by TEM-SAED analysis, for instance in the case of Fe-S:As (Figure SI-13), and semi-quantitative analyses of isolated pyrite grains are reported in Figures SI-14 to SI-19. The six analyzed samples presented a mixture of pyrite grains of different shapes and size in the submicron range, with an overall average size for each sample increasing in the order As < Mo < Ni < Co < Zn < Se. In all analyzed samples, cuboctahedral, octahedral and spheroidal particles were found to

coexist, these distinct shapes being attributed elsewhere to an increasing degree of supersaturation at room temperature, when shifting from a surface nucleation growth regime to a continuous growth processes (Wang and Morse, 1996). In all the samples analyzed by STEM-EDX, except for Fe-S:Ni that concentrates Ni in pyrite core (Morin *et al.*, 2017), the spatial distribution of the Co, Zn, Mo, As in the final pyrite grains collected at 3100 hours is homogeneous at the scale of the pyrite submicron grains (Figure 5). These observations suggest that the trace elements displayed in this figure are incorporated in the pyrite grains. In the case of Ni, a composite image is displayed in Figure SI-20, showing more details on the concentration of Ni in the core of the grains.

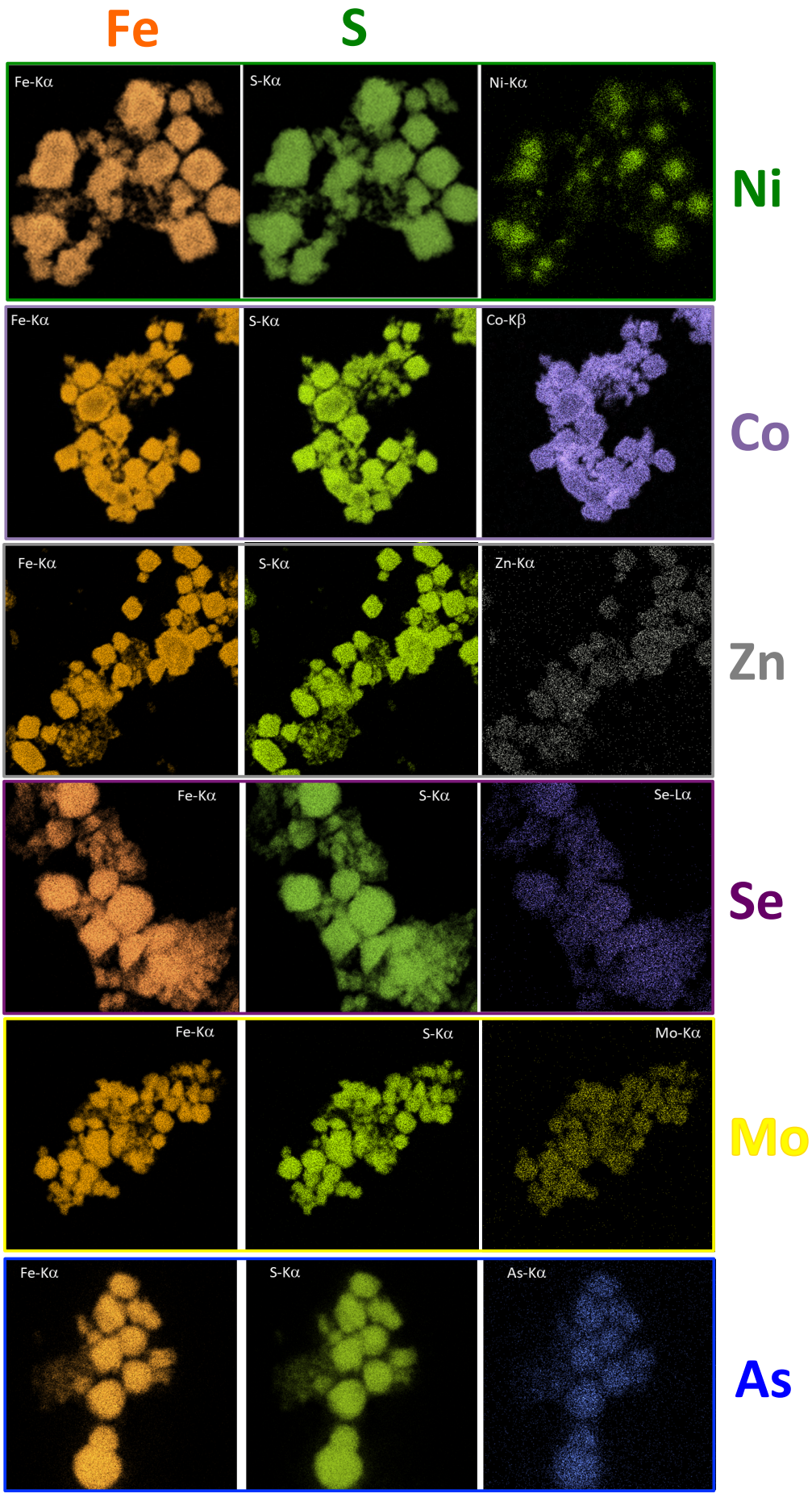
Fe
S
Fe-Kα
S-Kα
Ni-Kα
Ni
Fe-Kα
S-Kα
Co-Kβ
Co
Fe-Kα
S-Kα
Zn-Kα
Zn
Fe-Kα
S-Kα
Se-Lα
Se
Fe-Kα
S-Kα
Mo-Kα
Mo
Fe-Kα
S-Kα
As-Kα
As

Figure 5. *STEM-EDXS maps of the pyrite end-product of the synthesis experiments conducted in the presence of Ni, Co, Zn, Se, Mo or As. The elemental maps shows that Ni is mainly segregated at the cores of the pyrite grains, whereas the distribution of the other elements appears more homogeneous. Scale bar 1 µm. Complete STEM-HAADF figures are displayed in the supporting information (Figures SI-14 to SI-19).*

4. Discussion

4.1. Influence of trace elements on the kinetics of pyrite nucleation

According to previous studies having investigated pyrite syntheses via the polysulfide pathway at room temperature, rising up the synthesis pH from ~ 4 to 7 may slow down pyrite formation (Wang and Morse 1996; Wei and Osseo-Asare 1997). However, as detailed in section 3.2 and Fig. SI-11, initial pH values of 5.5 ± 0.3 were similar for all our experiments and evolved within the pH 5-6 range until the onset of pyrite formation, which supports the fact that the observed kinetic effects can be assigned to the added TEs rather than to pH differences. In our experiments, Cu, Zn, Se and V were found to exert no significant effect on pyrite formation kinetic. In contrast, Ni and, to a lesser extent, Mn and Co, accelerated pyrite formation, whereas As and Mo slowed it down. The observation of antagonistic effects of Ni and As on pyrite formation kinetic confirms previous results by Morin *et al.* (2017) and Baya *et al.* (2021) and reinforces the interest in evaluating the possible role of such kinetic effects in the geochemical behavior of these two elements in sulfidic systems. To this regard, our study confirms that Ni was efficiently sequestered in the solids from the beginning of the syntheses and it shows that a non-negligible portion of As remained in solution by the end of the experiment (~50-60%). This latter result could be related to the complex speciation of arsenic in sulfidic systems, since As can form aqueous thio-As molecules (Wilkin *et al.*, 2003) as further discussed in section 4.2. Moreover, both the persistence of a large fraction of As in the liquid phase and the delay in arsenian pyrite formation calls into question the ability of pyrite and other iron sulfides (Burton *et al*., 2011) to limit arsenic mobility during early diagenesis of modern sediments (Le Pape *et al.*, 2017; Asta *et al*., 2019).

Accelerated pyrite formation in the presence of aqueous Ni^{2+} has been extensively described by Morin *et al.* (2017) and Baya *et al*. (2021). This kinetic effect has been explained by the early formation of Ni-rich $(Fe,Ni)S_2$ nuclei detected by EXAFS analysis at the Ni *K*-edge before pyrite could be detected by XRD (Morin *et al*., 2017). This nucleation step is followed by pyrite crystal growth with a lower Ni/Fe ratio, leading to the observed zoning of the pyrite sub-micron grains (Morin *et al*., 2017). In preliminary syntheses in the presence of

475 Co performed by Noël (2014), with approximately two times more Co than in this study, a
476 stronger acceleration of pyrite formation was shown. Our results also agree with those of Noël
477 (2014) on the fact that Co was captured in the FeS solid fractions from the beginning of the
478 reaction and was efficiently sequestered by pyrite. According to STEM-EDXS mapping
479 performed in the present study, the Co-doped pyrites grains did not display any chemical
480 zoning (Figure 5, Figure SI-15), contrary to Ni (Figure 5, Figure SI-20)(Morin *et al.* 2017). In
481 our syntheses, the presence of Mn in the initial solution slightly accelerated pyrite formation,
482 which has not been documented yet. Especially, Noël (2014) did not observe this kinetic
483 effect in their preliminary pyrite synthesis conducted with two times more Mn, which
484 behaved similarly as their control experiment. Since Mn happens to be among the elements
485 frequently associated with sedimentary pyrite (Gregory *et al.*, 2015a), further studies will be
486 required to understand our results, and to better characterize the status of Mn in sedimentary
487 pyrite and the factors that control Mn scavenging by this mineral, as further discussed in
488 Section 4.2.

489 Pyrite particles formed in the presence of Mo appeared to be of small size compared to
490 those formed in the presence of the other trace elements, which may be related to the
491 inhibiting role we observed for Mo on pyrite formation kinetic. Bostick *et al.* (2003) have
492 determined that MoS_4^{2-} can be adsorbed irreversibly at the pyrite surface at pH<6 in the form
493 of stable Mo-Fe-S cubane clusters. Although Mo exhibits an affinity with FeS as observed by
494 Vorlicek *et al.* (2004) and Helz *et al.* (2004), it might be expulsed from the solids a few hours
495 after its uptake, as polysulfides are consumed during recrystallization of FeS into
496 mackinawite/greigite (Helz *et al.*, 2004). Such a sorption of Mo onto both FeS and FeS_2 could
497 explain that Mo inhibited pyrite formation in our Fe-S:Mo synthesis experiment, as further
498 discussed in section 4.2. The progressive release of Mo observed into the solution at the end
499 of the lag phase could have finally permitted FeS conversion into pyrite.

500 Pyrite particles formed in the presence of Se appeared to have larger sizes than in the
501 presence of the other trace elements and Se was homogeneously distributed in the pyrite sub-
502 micron crystals. We did not observe any effect of Se on pyrite formation rate, which contrasts
503 with the finding of Diener and Neumann (2011) who have reported a zoning of Se in their
504 synthetic micro-size pyrite grains under FIB-TEM-EDX examination. This difference could
505 be possibly related to the higher Se/Fe ratio in their syntheses, with initial Se molarity up to
506 1 mM.

4.2. Pyrite formation processes and mechanisms of trace metal incorporation

Except for Fe-S:Ni, the STEM-EDXS analyses performed on the 3100 h samples for Fe-S:Co, Fe-S:Zn, Fe-S:Se, Fe-S:As and Fe-S:Mo did not display any heterogeneity nor core enriched in the added TE. The results observed in the Fe-S:Ni experiment are in agreement with previous works from Morin *et al.* (2017) which have shown similar Ni enrichment at the core of pyrite grains. In the other experiments (Figure 5), the absence of chemical zonation implies that pyrite crystallites grew from aqueous species or from FeS precursors (Puthussery *et al.*, 2011; Bi *et al.*, 2011) with a constant amount of trace element incorporated in their structures over time. Such aqueous species could include pyrite clusters with size smaller than the critical precipitation nucleus (Wang and Morse, 1996). As the observed nucleation phase is rapid after the initial lag phase (Morin *et al.*, 2017; Baya *et al.*, 2021), we propose that burst nucleation occurred as a result of a gradual supersaturation increase in Fe and S species involved in pyrite formation (Rickard, 2019). During the nucleation phase, the FeS_2 nuclei would precipitate to give birth to crystallites that could further connect through oriented attachment (Zhu *et al.*, 2015), possibly using initial FeS particles as templates (Puthussery *et al.*, 2011; Bi *et al.*, 2011). Indeed, SEM images from our previous studies (Le Pape *et al.*, 2017; Baya *et al.*, 2021) showed that pyrite sub-micron grains obtained via similar synthesis procedure are constituted of crystallites of smaller size (20-50 nm). A relative monodisperse distribution of pyrite particles would also be compatible with this aggregation process (Zhu *et al.*, 2015). However, the presence of a Ni-rich $(Ni,Fe)S_2$ core surrounded by a Ni-depleted $(Fe,Ni)S_2/FeS_2$ overgrowth (Morin *et al.*, 2017) in the submicron pyrite grains grown in the presence of Ni^{2+}, suggests that a rapid growth stage from ionic aqueous species could follow the initial aggregation of pyrite nuclei, leading to efflorescent shapes observed by SEM (Baya *et al.,* 2021). Eventually, Ostwald ripening cannot be excluded after the aggregation and rapid growth stages. Though, we observed that the final submicronic particles remarkably conserved the same size and morphology after aging in the Fe(II)-rich solution (Baya *et al.*, 2021).

Generally, Mn is not observed to be abundant in natural pyrite (Tribovillard *et al.*, 2006; Large *et al.*, 2017) even if there are few evidences of important Mn enrichment in sedimentary pyrite at particularly high degree of pyritization corresponding to high Mn/Fe ratio in the precipitating media (Huerta-Diaz and Morse, 1992; Shikazono *et al.*, 1994). As the Mn sulfide phases (MnS/MnS_2) exhibit a high solubility (Kornicker and Morse, 1991), Mn^{2+} interacts with mackinawite FeS mainly by sorption, the magnitude of which decreases with

salinity (NaCl) and precipitation rate of FeS (Arakaki and Morse, 1993). In contrast, sorption of Mn^{2+} on pyrite surfaces is limited (Kornicker and Morse, 1991). In a recent study, Lin *et al.* (2022) have synthesized pyrite at the 1/9 Mn(II)/Fe molar ratio at 160°C from pre-precipitated amorphous FeS in the presence of Mn and S(0), which resulted in the incorporation of Mn in pyrite in the cores of the particles. This result, contrasting with our study and evoking our observation with Ni (Morin *et al.*, 2017 and this study), stresses that temperature is an important kinetic factor to take into account for Mn incorporation in pyrite, as well as NaCl concentration in the media.

Only few data are available on the mechanisms of Co precipitation at low temperature in the presence of iron and sulfides. In agreement with the general view (Huerta-Diaz and Morse, 1992; Arakaki and Morse, 1993; Swanner *et al.*, 2019), a recent study by Mansor *et al.*, (2020) indicated that, in the presence of an excess of sulfides and Fe, Co precipitates as Co-rich FeS. Other possible discrete Co-sulfide phases such as more or less amorphous and non-stochiometric CoS, can also potentially serve as host for Co (Mansor *et al.*, 2020). In addition, it cannot be excluded that other Co-sulfide such as linnaeite (Co_3S_4) or cattierite (CoS_2) play a role in Co distribution. Since Co is commonly enriched in sedimentary pyrites (*e.g.* Scholz and Neumann, 2007; Qiu *et al.*, 2021) it has been tentatively used to track changes in marine redox evolution (Swanner *et al.*, 2014). Lin *et al.* (2022) synthesized pyrite nanoparticles at high temperature in the presence of Co, which presented a homogeneous Co distribution at the particle scale comparable to our observation in the present study (Figure 5). This distribution contrasted with that of Ni and Mn, which presented enriched cores in the study by Lin *et al.* (2022). In our study, no Co was released to the solution during the whole reaction sequence, showing that it remained trapped within the solids. Determining the step-by-step evolution of Co speciation would be required to unambiguously identify the Co phase-transfer processes accompanying the FeS to FeS_2 transformation.

In the presence of dissolved sulfides, Cu precipitate as covellite (CuS) and form Cu-S dissolved monomers (Shea and Helz, 1988, 1989). When both iron and sulfide are present in the media at ambient temperature, diverse Cu-bearing species can form depending on the Cu/Fe ratio (Mansor *et al.*, 2019). For instance, Zavašnik *et al.* (2014) have observed Cu incorporation into amorphous FeS at low Cu loading, while chalcopyrite $(Cu, Fe)S_2$ can also form at low temperature, resulting from the maturation of precursor Fe-Cu-S phases (Cowper and Rickard, 1989; Mansor *et al.*, 2019). As for Ni (Ikogou et al., 2017), When Cu incorporates into FeS, it is found to improve its cristallinity upon aging (Zavašnik *et al.*, 2014;

573 Mansor *et al.*, 2019). In natural pyrite, Cu was mainly reported to occur as Cu-Fe sulfide
574 inclusions (Reich *et al.*, 2013) or more rarely as a substituting Cu^{2+} ion both at high
575 temperature (Schmid-Beurmann and Bente, 1995) or when forming from Fe-Cu sulfide
576 phases at low temperature (Pačevski *et al.*, 2008). Cu incorporation in pyrite locally distorts
577 the octahedral site, and increases the cell parameter (Pačevski *et al.*, 2008). In the conditions
578 of our experiment, it is likely that Cu first incorporates into FeS precursors, whereas both a
579 CuS_2-FeS_2 solid solution or a Fe-Cu sulfide phase inclusions could be envisaged in our final
580 pyrite sample. The transformation should occur at the solid state as exemplified in Zavašnik *et*
581 *al.* (2014), which would be consistent with the full retention of Cu within the solid during the
582 experiment (Figure 3, Figure 4).
583 ZnS is often observed in continental sediments, even in the presence of Fe or pyrite in
584 the media (Priadi *et al.*, 2012), which may be explained by the low solubility of this mineral.
585 According to (Labrenz *et al.*, 2000), even in the presence of Fe at natural concentrations in
586 surface waters, Zn quickly binds to sulfides from solution and forms ZnS particles, thus
587 preventing any further FeS or FeS_2 formation. Considering the fact that ZnS is much less
588 soluble than FeS (Rickard and Luther, 2006), we infer that, in our experiment, Zn first
589 precipitated as ZnS in the presence of FeS, even if Fe concentration is 2 orders of magnitude
590 higher than that of Zn. However, it cannot be excluded that Fe partly substitutes within the
591 ZnS structure (Lepetit *et al.*, 2003). This particular stability of ZnS is also illustrated by the
592 occurrence of ZnS particles in mixture with pyrite subunits within framboids (Hu *et al.*,
593 2018). In this latter study, the authors showed that Zn could be found both as trace element in
594 the pyrite subunits as well as ZnS particles. Here, Zn distribution at the crystal scale appears
595 homogeneous (Figure 5), which suggests Zn incorporation within pyrite, though the
596 occurrence of nano-ZnS particles cannot be excluded at our scale of observation.
597 Interestingly, we observed a release of Zn in solution during pyritization, which might be
598 related to ZnS destabilization due to Fe and S uptake required for pyrite burst nucleation. This
599 observation, pointing potentially to a particular mechanism for pyrite formation in the
600 presence of this trace element, could have important implications for the cycling of this
601 essential nutrient, and thus deserves further research.
602 Selenide, having a close ionic radii and similar charge to sulfide, is likely to replace it
603 in the structure of sulfide minerals, including in iron sulfides (Charlet *et al.*, 2012; Diener *et*
604 *al.*, 2012). Thus, in the presence of selenide, FeS was shown to incorporate Se as Se(-II) at the
605 S(-II) sites with no Se(0) or clustering detected by EXAFS at the Se K-edge for a sample with

606 1/100 Se/S ratio (Finck *et al.*, 2012). In our experiment, Se was introduced as selenate Se(VI),
607 which implies a first step of reduction by sulfides before incorporation, and then possible
608 combination of coprecipitation and sorption to FeS. In previous studies, when Se is sorbed to
609 the FeS surface, a mixture of Se(-II) and Se(0) was observed and shell-by-shell fits of EXAFS
610 data included Se-Se distances (Breynaert *et al.*, 2008; Finck *et al.*, 2012). In natural pyrite, Se
611 has been mainly described as Se(0) incorporating at S sites even if local clustering (Se-Se
612 pairs) cannot be excluded according to XAS results (Liu *et al.*, 2008; Charlet *et al.*, 2012;
613 Manceau *et al.*, 2020). Using micro-EXAFS on shale samples, Ryzer *et al.* (2005) reported
614 two types of Se speciation, one close to Se-pyrite, and another one close to ferroselite ($FeSe_2$).
615 Accordingly, Matamoros-Veloza *et al.*, (2014), also using micro-EXAFS measurements,
616 concluded on the presence of the classical Se to S substitution in euhedral pyrite particules but
617 also identified a $FeSe_x$ phase close from ferroselite ($FeSe_2$), found particularly in framboidal
618 pyrite particles. In our case, TEM-EDXS results showed a relatively homogeneous
619 distribution of Se in the pyrite particles with Se remaining in the solid phases during the
620 whole reaction sequence. Further EXAFS analysis at the Se K-edge of our solids would be
621 necessary to conclude on molecular scale Se distribution.
622 Very few data are available on the mechanisms of V scavenging by iron sulfides. A
623 recent study by Vessey and Lindsay (2020), relying on XAS results at the V K-edge, showed
624 that in the presence of mackinawite in solution, V(V) is reduced to V(IV)/V(III) according to
625 the analysis of centroid position and area of the pre-edge XANES peak. Further EXAFS shell-
626 by-shell analysis gave evidence for S atoms in the first shell around the V absorber. This
627 means that V can at least sorb to FeS as inner-sphere complex, and/or can possibly
628 incorporate into FeS particles. On this basis, and considering the rapid V precipitation
629 occurring in our experiment (Figure 3), we hypothesize that V was rapidly trapped by FeS
630 species through V for Fe substitution and/or surface sorption. In Earth's surface
631 environments, such as black shales or hydrothermal deposits, V is moderately enriched in
632 pyrite compared to the surrounding matrix (Franchini *et al.*, 2015; Large *et al.*, 2017). Indeed,
633 as U and Mo, this element is generally ascribed to its association with organic matter in
634 euxinic conditions (Tribovillard *et al.*, 2006). Accordingly, in Vessey and Lindsay (2020) the
635 authors show that V uptake by pyrite surfaces in sorption experiment is very limited. In our
636 study, V is trapped in the solid phase during the whole experiment, showing that V interaction
637 with iron sulfides may be an important process limiting the mobility of this element in anoxic

environments. However, to our knowledge, the actual mode of incorporation and redox state of V during the pyritization sequence remains unknown.

Mo speciation in environmental samples representative of sulfidic/euxinic conditions has been extensively studied, including by XAS at the Mo K-edge (Helz *et al.*, 2004; Dahl *et al.*, 2013; Chappaz *et al.*, 2014; Vorlicek *et al.*, 2018). However, few data are currently available on Mo speciation in dynamic synthetic systems precipitating Fe-sulfides, which reinforces the framework proposed here to study the evolution of Mo speciation during our reaction sequence. In the presence of large amount of Fe and S such as in our experiments, FeS minerals can scavenge efficiently thiomolybdate forms by sorption (Helz *et al.*, 2004), but Mo is rather expected to form colloidal Fe-Mo-S « cubane » type clusters and to stabilize in the $FeMoS_4$ form (Helz *et al.*, 1996; Vorlicek *et al.*, 2018). Additionally, the presence of $S(0)/S_n^{2-}$ in the medium have been shown to cause a ligand-induced reaction stabilizing thiomolybdate Mo(VI) into Mo(IV) monomer or Mo(V) dimer forms (Vorlicek *et al.*, 2004). In sediments, Mo is detected in pyrite, but this mineral might not be the main carrier phase in anoxic/sulfidic conditions (Chappaz *et al.*, 2014) since thiolated organic matter could also be an important scavenging agent (Helz *et al.*, 1996; Tribovillard *et al.*, 2004; Wagner *et al.*, 2017). Sorption experiments carried out on pyrite surfaces converge to the idea that thiomolybdate can strongly bind as inner-sphere complexes, which further maturate towards Fe-Mo-S cubane conformation upon aging (Bostick *et al.*, 2003; Vorlicek *et al.*, 2004). However, no direct observation of Mo speciation at the molecular scale in pure pyrite is currently available. In our pyrite synthesis experiment performed at ambient temperature, Mo is first quickly trapped by the solid phase before being slowly released in solution, and this before pyrite precipitation. Like for As, we can hypothesize that the presence of thiomolybdate forms as well as of cubane like Fe-Mo-S species can poison pyrite nucleation by precluding $S(0)/S_n^{2-}$ interactions with Fe_xS_x clusters, finally resulting in the observed lag phase before pyrite precipitation.

When coprecipitated with FeS, As forms amorphous As_2S_3-like species, or/and possibly soluble thio-As molecules sorbed to the FeS surfaces (Couture *et al.*, 2013; Le Pape *et al.*, 2017; Baya *et al.*, 2021). In pyrite, As can substitute at both S tetrahedral site as As(-I) (Savage *et al.*, 2000) and Fe octahedral site as As(II/III) (Deditius *et al.*, 2008; Qian *et al.*, 2013). A previous study on the same type of FeS_2 synthesis as in the present study has shown that As substitutes at both the S and Fe sites without excluding the possibility of As clustering (Le Pape *et al.*, 2017). Here, we bring additional data from TEM-EDXS showing an apparent

671 homogeneous distribution of As atoms/clusters at the particle scale (Figure 5 and Figure SI-
672 19). As shown in the literature, As poisons pyrite formation (Wolthers *et al.*, 2007; Le Pape *et*
673 *al.*, 2017; Baya *et al.*, 2021), which is also observed in the present study. Additionally, we
674 show here that an important part of As remains in solution through the whole reaction
675 sequence, and thus does not associate to the precipitated solids. First, As concentration
676 dropped, possibly due to its precipitation as As-sulfide, then it was released into solution, as
677 potentially driven by the thio-As/am-As_2S_3 equilibrium (Wilkin *et al.*, 2003; Le Pape *et al.*,
678 2017), and finally, a portion of As in solution was trapped when pyrite precipitation occurred,
679 attesting of a little but significant uptake.

680 **4.3. Extent of trace element incorporation and comparison with natural pyrites**

681 In studies focusing on the chemical composition and zonation of pyrite nodules, Ni is
682 systematically found to be enriched in the nodule core that is hypothesized to be the initial
683 early diagenetic precipitate (Marin-Carbonne *et al.*, 2014; Li *et al.*, 2017). Recently,
684 enrichment in trace elements such as Ni and As were also observed in the core of pyrite
685 nodules of Kapai Slate shales from western Australia (Chen and Campbell, 2021). These
686 researchers proposed that the nodule core have recorded the trace element composition of
687 water at the time of pyrite formation, and ranked their affinity with pyrite as Bi > Te > Sb >
688 Ag > Cu > Pb > Ni≈As > (Co, Zn, Se, Cd, Mn, W) > Tl > Mo. Besides, Gregory *et al.*
689 (2015a) reported the following ranking of trace elements abundance in sedimentary pyrites as
690 As ≥ Ni > Pb ≥ Cu ≥ Co ≥ Mn > Sb ≥ Zn ≥ Se ≥ Mo > Ag ≥ Bi > Te ≥ Cd > Au. In the present
691 study, the affinity of trace elements with pyrite can be drawn as Cu ≥ Ni ≥ Co > Se, Mo >>
692 As > Zn >> Mn (Figure 4). Thus, dramatic differences can be noted in elemental
693 compositions among natural sedimentary pyrites as well as among affinities determined form
694 various natural settings and laboratory experiments. This is particularly true for the affinities
695 for pyrite observed for As, Mn and Mo in our study compared to available literature.
696 While Mo harbors relatively high concentration in the oceanic water (Large *et al.*,
697 2014), low concentrations (<1ppm) are measured in the pyrite core nodules comparatively to
698 Ni (1000-1500 ppm) and As (up to around 1000 ppm) (Chen and Campbell, 2021). In our
699 study, we show that a part of Mo remained in solution, in particular after having first
700 precipitated, even if a relatively important amount is finally incorporated into the solids (~
701 20000 ppm). One possible bias is that in our case Mo can incorporate into pyrite in lower

concentration than estimated because of local precipitation of individual Mo-sulfides, although such phases could not be detected at the scale of our STEM-EDX observations.

Under our low-temperature synthesis conditions, we observed a significant affinity of V for the pyrite solid ($D \sim 47$), compared to much lower D values ($D \sim 1$) reported for hydrothermal conditions (Tauson *et al.*, 2017). This result calls for further assessing the possible role of iron sulfides in V cycling in sedimentary environments. However, it also emphasizes the variability of partitioning coefficients as a function of formation conditions, and, again questions the actual redox and structural status of V when associated to natural pyrites.

In our synthesis conditions, As showed a moderate affinity for pyrite while it is widely observed in sedimentary pyrite and it is the most concentrated element in this mineral, as reported by Gregory *et al.* (2015a). In the same way, the solid/liquid partition coefficient we observe ($D \sim 3$) is about a hundred-fold lower than that observed in hydrothermal pyrite synthesis experiments (Kusebauch *et al*., 2018). Several hypotheses can be raised to explain this difference. First, high concentration of As such as in our experiments may lower the D value, as previously reported by Kusebauch *et al*. (2018). Besides, the lower temperature used here delays As incorporation in arsenian pyrite (Figure 1), as previously reported by Le Pape *et al*. (2017) and Baya et al. (2021). In addition, high As loading can potentially inhibit the dynamics of pyrite nucleation mediated by polysulfides, for instance by forming dissolved thio-As species (Baya *et al.*, 2021). Eventually, in natural waters, it could be inferred that the concomitant presence of accelerating elements such as Ni can help As to enter in the pyrite structure. Indeed, both elements are widely observed in sedimentary pyrites, and sometimes present correlation in their enrichment, for instance in organic matter rich shales (Dill and Kemper, 1990).

Finally, the difference observed between our results and those derived from natural settings is particularly striking for Mn. In our experiment, pyrite is devoid of Mn that fully remains in solution, while Mn is typically observed in the ~1000-2000 ppm range in sedimentary pyrite nodules (Large *et al.*, 2014). The frequent occurrence of Mn in natural pyrite as well as the ability of Mn to be incorporated in synthetic hydrothermal pyrites contrasts with our present results that are in line with the preliminary data from Noël (2014) that showed no association of Mn^{2+} with the solid phase during room temperature synthesis of pyrite. Among various factors, increasing temperature (Lin *et al.,* 2022) and Mn/Fe ratio (Huerta-Diaz and Morse, 1992; Shikazono et al., 1994) may favor the incorporation of Mn in

pyrite. One may also hypothesize again that complex chemistry of natural systems might permit synergistic effects between trace elements, such as pairing or clustering of cations with anions that could perhaps help their insertion in pyrite. For instance, pure $MnSe_2$ with the pyrite structure can be rapidly produced (12 h) at moderate temperature (100°C) (Wu *et al.*, 2004). Thus, our results should motivate the study of the co-insertion of both elements in pyrite under diagenetic conditions.

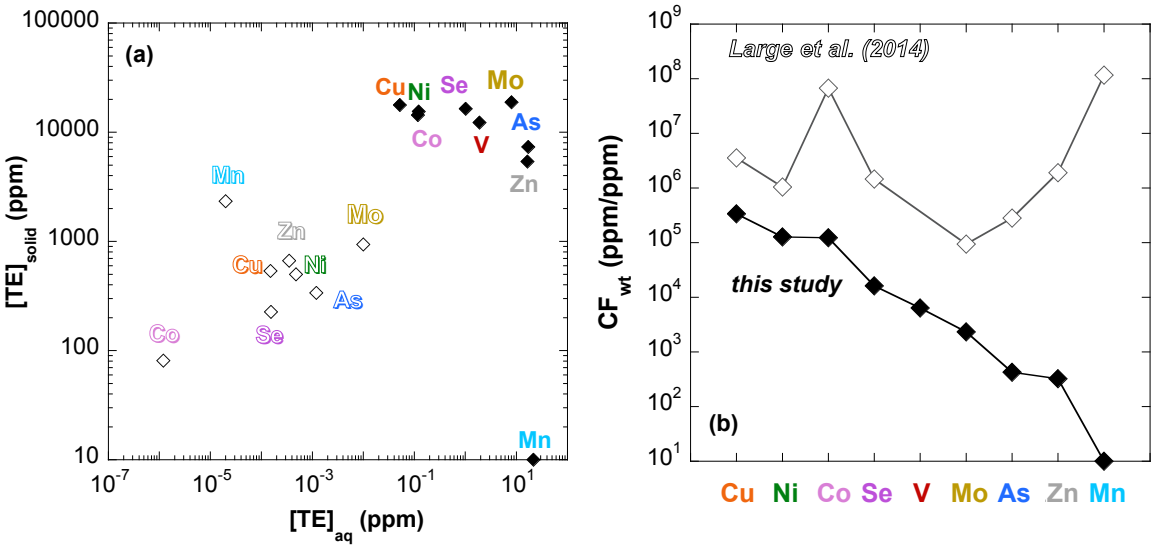

Figure 6. *Comparison of our experimental solid-solution partition results (close diamonds) with those reported by Large et al. (2014) for natural pyrites vs. seawater (open diamonds). Left: TE concentration in the solid phase ([TE]solid in ppm wt.) as a function of TE concentration in the aqueous phase ($[TE]_{aq}$ in mg.L-1). Right: Concentration Factor (CF) calculated as the ratio of $[TE]_{solid}$ / $[TE]_{aq}$ (in ppm/ppm). The CF values measured in this study are compared to those reported by Large et al. (2014), all data given in ppm/ppm unit, i.e., without applying the 10^{-4} of Large et al. (2014).*

In order to directly compare our results within the frame of a solid-solution partition between natural waters and pyrite, we calculated the concentration factors of the trace elements in our synthetic pyrites solids within the framework proposed by Large *et al.* (2014), but without dividing by 10^4, which yields: $CF = [TE]_{py} / [TE]_{aq}$ (ppm wt. / ppm wt.). We thus compare the concentration factors in our final solids (Table SI-1 and Figure 6) to those obtained by Large *et al.* (2014) between mean ocean seawater and sedimentary pyrites from the Cariaco Basin.

While Cu and Ni exhibit comparable concentration factors in both studies (Figure 4, right) albeit with one order of magnitude difference, the concentrations factors of the other trace elements do not match those of Large *et al.* (2014) that are several orders of magnitude higher than in the present study. A main factor that likely explains the dramatic mismatch

between our experimental results and the enrichment factors calculated from natural setting is that our final aqueous TE concentrations are about 3 to 6 orders of magnitudes higher than those in ocean waters (Figure 6, left). However, the amounts of TE incorporated in pyrite in our experiments are only 1 to 2 orders of magnitude higher than in natural sedimentary pyrites, which yields the large mismatch in the concentration factors (Figure 6, right). Our study might thus, at most, be rather considered as representative of the solid-solution partition between pyrite and sediment pore-waters than with ocean or lake water columns. For instance, aqueous Ni may occur within the 0.4 - 2.9 ppm range in pyrite-rich mangrove sediment pore-waters (Noel et al. 2015), which is consistent with the 0.1- 0.2 ppm range of aqueous Ni concentrations in our experiments after pyrite synthesis (Table SI-1). Lowering the initial amount of TE added in the synthesis medium of one or two orders of magnitude would allow to better match a broader variety of natural environments. Nevertheless, the present study yields a reliable methodological frame to directly measure pyrite-water TE partition at room temperature in conditions relevant to early diagenesis. Another apparent limitation of the applicability of our results to natural environments could be the relatively acidic pH of our synthesis media (pH 4-6). Nevertheless, this pH range is consistent with typical successful synthesis conditions for pyrite via the polysulfide pathway at room temperature, e.g. pH 5-7 in Wang and Morse (1996) or pH 3.6-6.5 in Wei and Osseo-Asare (1997). Besides, it is likely that local pH conditions that permit pyrite nucleation in sediment micro-environments might be actually acidic, as for instance in mangrove sediments (pH 5-6, Noel et al., 2014). Eventually, our experiments did not account for the combined effect of trace element on their mutual incorporation in pyrite, as discussed above for Ni and As.

Besides, approaches based on direct comparison of modern sedimentary pyrite composition with that of ocean water, as proposed by Large *et al.* (2014), may also be limited since the TE composition of seawater is actually not only controlled by pyrite but also by other phases especially clay minerals, oxyhydroxides and carbonates. For instance, Baldermann *et al.* (2015) have shown the importance of green-clay authigenesis in the sequestration of Fe in modern deep-sea sediments. Moreover, (Merrot *et al.*, 2019) reported that such a process can also largely control the fate of Ni in lagoon sediments, while carbonates play a key role in sequestrating Mn in the same environments (Merrot *et al.*, 2021). Additionally, recent works from Chen and Campbell (2021) have shown that the enrichment factors depicted by Large *et al.* (2014) and Mukherjee and Large (2020), e.g. for

Mn and Mo, potentially entail some uncertainties such as the values of mean ocean concentrations, and the high variability of Cariaco pyrite chemical composition.

Here, we provide for the first time values of solid-liquid partition for trace elements in pyrite synthesized via the polysulfide pathway in laboratory-controlled conditions. Even if the approach is simplified and cannot be directly compared to complex natural environments, we provide a reliable methodological framework to study TE partition over the course of a whole reaction sequence leading to pyrite formation. Thus, our experiments, involving pyrite formation via the polysulfide pathway, aimed at approaching early diagenetic conditions representative of the formation of first grains of pyrite as it possibly occurs within newly deposited sediment. It helps to classify the affinities of each individual trace element with pyrite, which is not directly feasible with natural pyrites as precipitating solution is complex and its chemical composition can only remain hypothetical (Chen and Campbell, 2021).

5. Conclusion

The aim of this work was to provide a methodological framework to comparatively study the affinities of some trace metals and metalloids for the solid phases along the reaction sequence leading to pyrite formation in low-temperature environments and to evaluate the kinetic effects related to their presence. The major findings of this study are that the addition of Ni and to a lesser extent of Mn and Co accelerate pyrite formation, V, Cu, Zn and Se have no significant effect, and As and Mo significantly delay it. Additionally, we depict the partition of trace elements between the solid and the liquid phase over the course of pyrite formation: while Ni, Co, Cu and Se are quickly scavenged within the solids and remained as is until the end of the experiment, Mn is observed to mainly remain in solution. Arsenic is only partly sequestered from the beginning while Zn and Mo are first sequestered and are then partly released in solution. The STEM-EDXS analysis of the Co-, Se-, Zn-, As- and Mo-bearing final pyrites show an homogeneous TE distribution at the submicron particle scale, most likely attesting that pyrite formation has not been favored by the formation of TE-rich nuclei as observed for Ni. In the literature, most works on pyrite associations to these elements have been performed at high temperatures and/or via adsorption experiments on previously-formed FeS or FeS_2. A particular contribution of this study is that the syntheses were performed at low temperatures, in conditions that could be comparable to early diagenesis in continental or marine sediments. Moreover, the complex but relevant reaction sequence proposed here is particularly suited to monitor the speciation of trace elements,

824 which could undoubtedly fill some literature gaps on trace element speciation during
825 pyritization. However, a better matching to natural conditions will require to investigate
826 similar systems with much lower initial concentrations of trace elements in order to better
827 mimic solid-solution partition occurring during pyrite formation in sedimentary environments.
828 In this perspective, such further studies may benefit of the methodological framework
829 developed here as well as of the results of the present work concerning kinetic effects of trace
830 elements on pyrite formation.

831 ## 6.Acknowledgements

832 The authors are indebted to Sorbonne University Licence Students, Chaïma Bentabet,
833 Heloïce Mukuna and Abdramane Traoré who have helped to prepare the syntheses solutions
834 during their 10 days internship at IMPMC. The authors thank ED 398, MESR and Sorbonne
835 University for having provided the PhD grant of C. Baya. We are also indebted to the IMPMC
836 project cell, including Gilles Lemarchand, Yiuri Garino and Philippe Rosier for
837 implementation of μXRD and μFluoX computer interfaces.
838

7.References

Arakaki T. and Morse J. W. (1993) Coprecipitation and adsorption of Mn(II) with mackinawite (FeS) under conditions similar to those found in anoxic sediments. *Geochimica et Cosmochimica Acta* **57**, 9–14

Asta M., Wang Y., Frutschi M., Viacava K., Loreggian L., Le Pape P., Vo P.L., Fernandez A.M., Morin G., Bernier-Latmani R. (2019) Microbially-mediated release of As from Mekong Delta peat sediments. *Environmental Science and Technology* 53, 10208-10217

Baldermann A., Warr L. N., Letofsky-Papst I. and Mavromatis V. (2015) Substantial iron sequestration during green-clay authigenesis in modern deep-sea sediments. *Nature Geoscience* **8**, 885–889.

Baya C., Le Pape P., Baptiste B., Brest J., Landrot G., Elkaim E., Noël V., Blanchard M., Ona-Nguema G., Juillot F. and Morin G. (2021) Influence of trace level As or Ni on pyrite formation kinetics at low temperature. *Geochimica et Cosmochimica Acta* **300**, 333–353.

Benning L. G., Wilkin R. T. and Barnes H. L. (2000) Reaction pathways in the Fe–S system below 100°C. *Chemical Geology* **167**, 25–51.

Berner R. A. (1964) Iron Sulfides Formed from Aqueous Solution at Low Temperatures and Atmospheric Pressure. *The Journal of Geology* **72**, 293–306.

Berner R. A. (1984) Sedimentary pyrite formation: An update. *Geochimica et Cosmochimica Acta* **48**, 605–615.

Berner R. A. (1967) thermodynamic stability of sedimentary iron sulfides. *American Journal of Science* **265**, 773–785.

Bertine K. K. (1972) The deposition of molybdenum in anoxic waters. *Marine Chemistry* **1**, 43–53.

Bi Y., Yuan Y., Exstrom C. L., Darveau S. A. and Huang J. (2011) Air stable, photosensitive, phase pure iron pyrite nanocrystal thin films for photovoltaic application. *Nano Letters* **11**, 4953–4957.

Bostick B. C. and Fendorf S. (2003) Arsenite sorption on troilite (FeS) and pyrite (FeS2). *Geochimica et Cosmochimica Acta* **67**, 909–921.

Bostick B. C., Fendorf S. and Helz G. R. (2003) Differential Adsorption of Molybdate and Tetrathiomolybdate on Pyrite (FeS2). *Environmental Science and Technology* **37**, 285–291.

Breynaert E., Bruggeman C. and Maes A. (2008) XANES−EXAFS Analysis of Se Solid-Phase Reaction Products Formed upon Contacting Se(IV) with FeS2 and FeS. *Environmental Science and Technology* **42**, 3595–3601.

Butler I. B. and Rickard D. (2000) Framboidal pyrite formation via the oxidation of iron (II) monosulfide by hydrogen sulphide. *Geochimica et Cosmochimica Acta* **64**, 2665–2672.

Burton E.D., Johnston S.G., Bush R.T. (2011) Microbial sulfidogenesis in ferrihydrite-rich environments: Effects on iron mineralogy and arsenic mobility. *Geochimica et Cosmochimica Acta* 75, 3072-3087.

Chappaz A., Lyons T. W., Gregory D. D., Reinhard C. T., Gill B. C., Li C. and Large R. R. (2014) Does pyrite act as an important host for molybdenum in modern and ancient euxinic sediments? *Geochimica et Cosmochimica Acta* **126**, 112–122.

Charlet L., Kang M., Bardelli F., Kirsch R., Géhin A., Grenèche J.-M. and Chen F. (2012) Nanocomposite Pyrite–Greigite Reactivity toward Se(IV)/Se(VI). *Environmental Science Technology* **46**, 4869–4876.

887 Chen M. and Campbell I. H. (2021) Kinetic factors control trace element and isotope zoning
888 in Archean pyrite corona nodules. *Geochimica et Cosmochimica Acta*.
889 Couture R.-M., Rose J., Kumar N., Mitchell K., Wallschläger D. and Van Cappellen P. (2013)
890 Sorption of Arsenite, Arsenate, and Thioarsenates to Iron Oxides and Iron Sulfides: A
891 Kinetic and Spectroscopic Investigation. *Environmental Science Technology* **47**,
892 5652–5659.
893 Cowper M. and Rickard D. (1989) Mechanism of chalcopyrite formation from iron
894 monosulphides in aqueous solutions (< 100°C, pH 2–4.5). *Chemical Geology* **78**, 325–
895 341.
896 Dahl T. W., Chappaz A., Fitts J. P. and Lyons T. W. (2013) Molybdenum reduction in a
897 sulfidic lake: Evidence from X-ray absorption fine-structure spectroscopy and
898 implications for the Mo paleoproxy. *Geochimica et Cosmochimica Acta* **103**, 213–231.
899 Deditius A. P., Utsunomiya S., Renock D., Ewing R. C., Ramana C. V., Becker U. and Kesler
900 S. E. (2008) A proposed new type of arsenian pyrite: Composition, nanostructure and
901 geological significance. *Geochimica et Cosmochimica Acta* **72**, 2919–2933.
902 Denkhaus E. and Salnikow K. (2002) Nickel essentiality, toxicity, and carcinogenicity.
903 *Critical Reviews in Oncology/Hematology* **42**, 35–56.
904 Diener A. and Neumann T. (2011) Synthesis and incorporation of selenide in pyrite and
905 mackinawite. *Radiochimica Acta* **99**, 791–798.
906 Diener A., Neumann T., Kramar U. and Schild D. (2012) Structure of selenium incorporated
907 in pyrite and mackinawite as determined by XAFS analyses. *Journal of Contaminant*
908 *Hydrology* **133**, 30–39.
909 Dill H. and Kemper E. (1990) Crystallographic and chemical variations during pyritization in
910 the upper Barremian and lower Aptian dark claystones from the Lower Saxonian
911 Basin (NW Germany). *Sedimentology* **37**, 427–443.
912 Farquhar M. L., Charnock J. M., Livens F. R. and Vaughan D. J. (2002) Mechanisms of
913 Arsenic Uptake from Aqueous Solution by Interaction with Goethite, Lepidocrocite,
914 Mackinawite, and Pyrite: An X-ray Absorption Spectroscopy Study. *Environmental*
915 *Science and Technology* **36**, 1757–1762.
916 Finck N., Dardenne K., Bosbach D. and Geckeis H. (2012) Selenide Retention by
917 Mackinawite. *Environmental Science Technology* **46**, 10004–10011.
918 Franchini M., McFarlane C., Maydagán L., Reich M., Lentz D. R., Meinert L. and Bouhier V.
919 (2015) Trace metals in pyrite and marcasite from the Agua Rica porphyry-high
920 sulfidation epithermal deposit, Catamarca, Argentina: Textural features and metal
921 zoning at the porphyry to epithermal transition. *Ore Geology Reviews* **66**, 366–387.
922 Gregory D. D., Large R. R., Halpin J. A., Baturina E. L., Lyons T. W., Wu S., Danyushevsky
923 L., Sack P. J., Chappaz A., Maslennikov V. V. and Bull S. W. (2015a) Trace Element
924 Content of Sedimentary Pyrite in Black Shales. *Economic Geology* **110**, 1389–1410.
925 Gregory D. D., Large R. R., Halpin J. A., Steadman J. A., Hickman A. H., Ireland T. R. and
926 Holden P. (2015b) The chemical conditions of the late Archean Hamersley basin
927 inferred from whole rock and pyrite geochemistry with Δ33S and δ34S isotope
928 analyses. *Geochimica et Cosmochimica Acta* **149**, 223–250.
929 Hammersley A.P. (2016) FIT2D a multi-purpose data reduction, analysis and visualization
930 program. *Journal of Applied Crystallography* **49**, 646–652.
931 Helz G. R., Miller C. V., Charnock J. M., Mosselmans J. F. W., Pattrick R. A. D., Garner C.
932 D. and Vaughan D. J. (1996) Mechanism of molybdenum removal from the sea and its
933 concentration in black shales: EXAFS evidence. *Geochimica et Cosmochimica Acta*
934 **60**, 3631–3642.
935 Helz G. R., Vorlicek T. P. and Kahn M. D. (2004) Molybdenum Scavenging by Iron
936 Monosulfide. *Environmental Science and Technology* **38**, 4263–4268.

Hu S.-Y., Evans K., Rempel K., Guagliardo P., Kilburn M., Craw D., Grice K. and Dick J. (2018) Sequestration of Zn into mixed pyrite-zinc sulfide framboids: A key to Zn cycling in the ocean? *Geochimica et Cosmochimica Acta* **241**, 95–107.

Huerta-Diaz M. A. and Morse J. W. (1992) Pyritization of trace metals in anoxic marine sediments. *Geochimica et Cosmochimica Acta* **56**, 2681–2702.

Huerta-Diaz M. A., Tessier A. and Carignan R. (1998) Geochemistry of trace metals associated with reduced sulfur in freshwater sediments. *Applied Geochemistry* **13**, 213–233.

Ikogou M., Ona-Nguema G., Juillot F., Le Pape P., Menguy N., Richeux N., Guigner J.M., Noël V., Brest J., Baptiste B., Morin G. (2017) Long-term sequestration of nickel in mackinawite formed by Desulfovibrio capillatus upon Fe(III)-citrate reduction in the presence of thiosulfate. *Applied Geochemistry* **80**, 143-154.

Jean G. E. and Bancroft G. M. (1986) Heavy metal adsorption by sulphide mineral surfaces. *Geochimica et Cosmochimica Acta* **50**, 1455–1463.

Kornicker W. A. and Morse J. W. (1991) Interactions of divalent cations with the surface of pyrite. *Geochimica et Cosmochimica Acta* **55**, 2159–2171.

Kusebauch C., Oelze M., Gleeson S.A. (2018) Partitioning of arsenic between hydrothermal fluid and pyrite during experimental siderite replacement. *Chemical Geology* **500**, 136-147.

Labrenz M., Druschel G. K., Thomsen-Ebert T., Gilbert B., Welch S. A., Kemner K. M., Logan G. A., Summons R. E., Stasio G. D., Bond P. L., Lai B., Kelly S. D. and Banfield J. F. (2000) Formation of Sphalerite (ZnS) Deposits in Natural Biofilms of Sulfate-Reducing Bacteria. *Science* **290**, 1744–1747.

Large R. R., Danyushevsky L., Hollit C., Maslennikov V., Meffre S., Gilbert S., Bull S., Scott R., Emsbo P., Thomas H., Singh B. and Foster J. (2009) Gold and Trace Element Zonation in Pyrite Using a Laser Imaging Technique: Implications for the Timing of Gold in Orogenic and Carlin-Style Sediment-Hosted Deposits. *Economic Geology* **104**, 635–668.

Large R. R., Halpin J. A., Danyushevsky L. V., Maslennikov V. V., Bull S. W., Long J. A., Gregory D. D., Lounejeva E., Lyons T. W., Sack P. J., McGoldrick P. J. and Calver C. R. (2014) Trace element content of sedimentary pyrite as a new proxy for deep-time ocean–atmosphere evolution. *Earth and Planetary Science Letters* **389**, 209–220.

Large R. R., Mukherjee I., Gregory D. D., Steadman J. A., Maslennikov V. V. and Meffre S. (2017) Ocean and Atmosphere Geochemical Proxies Derived from Trace Elements in Marine Pyrite: Implications for Ore Genesis in Sedimentary Basins. *Economic Geology* **112**, 423–450.

Large R., Thomas H., Craw D., Henne A. and Henderson S. (2012) Diagenetic pyrite as a source for metals in orogenic gold deposits, Otago Schist, New Zealand. *New Zealand Journal of Geology and Geophysics* **55**, 137–149.

Le Pape P., Blanchard M., Brest J., Boulliard J.-C., Ikogou M., Stetten L., Wang S., Landrot G. and Morin G. (2017) Arsenic Incorporation in Pyrite at Ambient Temperature at Both Tetrahedral S^{-I} and Octahedral Fe^{II} Sites: Evidence from EXAFS–DFT Analysis. *Environmental Science and Technology* **51**, 150–158.

Lepetit P., Bente K., Doering T. and Luckhaus S. (2003) Crystal chemistry of Fe-containing sphalerites. *Physics and Chemistry of Minerals* **30**, 185–191.

Li J., Zhang Z., Stern R. A., Hannah J. L., Stein H. J., Yang G. and Li L. (2017) Primary multiple sulfur isotopic compositions of pyrite in 2.7Ga shales from the Joy Lake sequence (Superior Province) show felsic volcanic array-like signature. *Geochimica et Cosmochimica Acta* **202**, 310–340.

Liang Z-S., Song B-D., Liu Y-L., Liu Y., Ren H-T., Wu S-H., Jia S-Y., Han X. (2019) Reactivity Comparison of Different Ni(II)-Pyrites during Oxidative Dissolution under Acidic and pH-Neutral Conditions. *ACS Earth and Space Chemistry* **3**, 1096-1108.

Lin X., Xia Y., Wei G., Zhou J., Liang X., Xian H., Zhu J. and He H. (2022) Distinct effects of transition metal (cobalt, manganese and nickel) ion substitutions on the abiotic oxidation of pyrite: In view of hydroxyl radical production. *Geochimica et Cosmochimica Acta* **321**, 170–183.

Liu X., Fattahi M., Montavon G. and Grambow B. (2008) Selenide retention onto pyrite under reducing conditions. *Radiochimica Acta* **96**, 473–479.

Luther G. W. (1991) Pyrite synthesis via polysulfide compounds. *Geochimica et Cosmochimica Acta* **55**, 2839–2849.

McIntire W.L. (1963) Trace element partition coefficients - a reviw of theory and applications to geology. *Geochimica et Cosmochimica Acta* **27**, 1209-1264

Manceau A., Merkulova M., Mathon O., Glatzel P., Murdzek M., Batanova V., Simionovici A., Steinmann S. N. and Paktunc D. (2020) The Mode of Incorporation of As(-I) and Se(-I) in Natural Pyrite Revisited. *ACS Earth and Space Chemistry* **4**, 379–390.

Mansor M., Berti D., Hochella M. F. Jr., Murayama M. and Xu J. (2019) Phase, morphology, elemental composition, and formation mechanisms of biogenic and abiogenic Fe-Cu-sulfide nanoparticles: A comparative study on their occurrences under anoxic conditions. *American Mineralogist* **104**, 703–717.

Mansor M., Cantando E., Wang Y., Hernandez-Viezcas J. A., Gardea-Torresdey J. L., Hochella M. F. and Xu J. (2020) Insights into the Biogeochemical Cycling of Cobalt: Precipitation and Transformation of Cobalt Sulfide Nanoparticles under Low-Temperature Aqueous Conditions. *Environmental Science and Technology* **54**, 5598–5607.

Marin-Carbonne J., Rollion-Bard C., Bekker A., Rouxel O., Agangi A., Cavalazzi B., Wohlgemuth-Ueberwasser C. C., Hofmann A. and McKeegan K. D. (2014) Coupled Fe and S isotope variations in pyrite nodules from Archean shale. *Earth and Planetary Science Letters* **392**, 67–79.

Matamoros-Veloza A., Cespedes O., Johnson B. R. G., Stawski T. M., Terranova U., de Leeuw N. H. and Benning L. G. (2018a) A highly reactive precursor in the iron sulfide system. *Nature Communication* **9**, 3125.

Matamoros-Veloza A., Peacock C. L. and Benning L. G. (2014) Selenium Speciation in Framboidal and Euhedral Pyrites in Shales. *Environmental Science and Technology* **48**, 8972–8979.

Matamoros-Veloza A., Stawski T. M. and Benning L. G. (2018b) Nanoparticle Assembly Leads to Mackinawite Formation. *Crystal Growth & Design* **18**, 6757–6764.

Merrot P., Juillot F., Le Pape P., Lefebvre P., Brest J., Kieffer I., Menguy N., Viollier E., Fernandez J.-M., Moreton B., Radakovitch O. and Morin G. (2021) Comparative Cr and Mn speciation across a shore-to-reef gradient in lagoon sediments downstream of Cr-rich Ferralsols upon ultramafic rocks in New Caledonia. *Journal of Geochemical Exploration* **229**, 106845.

Merrot P., Juillot F., Noël V., Lefebvre P., Brest J., Menguy N., Guigner J.-M., Blondeau M., Viollier E., Fernandez J.-M., Moreton B., Bargar J. R. and Morin G. (2019) Nickel and iron partitioning between clay minerals, Fe-oxides and Fe-sulfides in lagoon sediments from New Caledonia. *Science of The Total Environment* **689**, 1212–1227.

Morin G., Noël V., Menguy N., Brest J., Baptiste B., Tharaud M., Ona-Nguema G., Ikogou M., Viollier E. and Juillot F. (2017) Nickel accelerates pyrite nucleation at ambient temperature. *Geochemical Perspective Let.*, 6–11.

1035 Morse J. W. and Arakaki T. (1993) Adsorption and coprecipitation of divalent metals with
1036 mackinawite (FeS). *Geochimica et Cosmochimica Acta* **57**, 3635-3640.
1037 Mukherjee I. and Large R. R. (2020) Co-evolution of trace elements and life in Precambrian
1038 oceans: The pyrite edition. *Geology* **48**, 1018–1022.
1039 Mukherjee I., Large R. R., Bull S., Gregory D. G., Stepanov A. S., Ávila J., Ireland T. R. and
1040 Corkrey R. (2019) Pyrite trace-element and sulfur isotope geochemistry of paleo-
1041 mesoproterozoic McArthur Basin: Proxy for oxidative weathering. *American*
1042 *Mineralogist* **104**, 1256–1272.
1043 Noël V. (2014) Speciation of iron and nickel in the mangrove sediments downstream
1044 lateritized ultramafic watershed (New Caledonia). PhD thesis, Université Pierre et
1045 Marie Curie (in french) pp 131-143. https://tel.archives-ouvertes.fr/tel-
1046 01140282/document
1047 Noël V., Morin G., Juillot F., Marchand C., Brest J., Bargar J. R., Muñoz M., Marakovic G.,
1048 Ardo S. and Brown G. E. (2015) Ni cycling in mangrove sediments from New
1049 Caledonia. *Geochimica et Cosmochimica Acta* **169**, 82–98.
1050 Pačevski A., Libowitzky E., Živković P., Dimitrijević R. and Cvetković L. (2008) Copper-
1051 bearing pyrite from the Coka Marin polymetallic deposit, Serbia: Mineral inclusions
1052 or true solid-solution? *The Canadian Mineralogist* **46**, 249–261.
1053 Parnell J., Perez M., Armstrong J., Bullock L., Feldmann J. and Boyce A. J. (2018)
1054 Geochemistry and metallogeny of Neoproterozoic pyrite in oxic and anoxic sediments.
1055 *Geochemical Perspectives Letters* **7**, 12–16.
1056 Poulton S. W. and Canfield D. E. (2011) Ferruginous Conditions: A Dominant Feature of the
1057 Ocean through Earth's History. *Elements* **7**, 107–112.
1058 Priadi C., Le Pape P., Morin G., Ayrault S., Maillot F., Juillot F., Hochreutener R., Llorens I.,
1059 Testemale D., Proux O. and Brown G. E. (2012) X-ray Absorption Fine Structure
1060 Evidence for Amorphous Zinc Sulfide as a Major Zinc Species in Suspended Matter
1061 from the Seine River Downstream of Paris, Ile-de-France, France. *Environmental*
1062 *Science and Technology* **46**, 3712–3720.
1063 Puthussery J., Seefeld S., Berry N., Gibbs M. and Law M. (2011) Colloidal Iron Pyrite (FeS2)
1064 Nanocrystal Inks for Thin-Film Photovoltaics. *Journal of the American Chemical*
1065 *Society* **133**, 716–719.
1066 Qian G., Brugger J., Testemale D., Skinner W. and Pring A. (2013) Formation of As(II)-
1067 pyrite during experimental replacement of magnetite under hydrothermal conditions.
1068 *Geochimica et Cosmochimica Acta* **100**, 1–10.
1069 Qiu Z.-J., Fan H.-R., Goldfarb R., Tomkins A. G., Yang K.-F., Li X.-C., Xie L.-W. and Liu
1070 X. (2021) Cobalt concentration in a sulfidic sea and mobilization during orogenesis:
1071 Implications for targeting epigenetic sediment-hosted Cu-Co deposits. *Geochimica et*
1072 *Cosmochimica Acta* **305**, 1–18.
1073 Raiswell R. and Canfield D. E. (1998) Sources of iron for pyrite formation in marine
1074 sediments. *American Journal of Science* **298**, 219–245.
1075 Raiswell R. and Plant J. (1980) The incorporation of trace elements into pyrite during
1076 diagenesis of black shales, Yorkshire, England. *Economic Geology* **75**, 684–699.
1077 Ratnaike R. N. (2003) Acute and chronic arsenic toxicity. *Postgraduate medical journal* **79**,
1078 391–396.
1079 Reich M., Deditius A., Chryssoulis S., Li J.-W., Ma C.-Q., Parada M. A., Barra F. and
1080 Mittermayr F. (2013) Pyrite as a record of hydrothermal fluid evolution in a porphyry
1081 copper system: A SIMS/EMPA trace element study. *Geochimica et Cosmochimica*
1082 *Acta* **104**, 42–62.
1083 Rickard D. (2019) How long does it take a pyrite framboid to form? *Earth and Planetary*
1084 *Science Letters* **513**, 64–68.

1085 Rickard D. and Luther G. W. (2007) Chemistry of Iron Sulfides. *Chemical Reviews* **107**, 514–
1086 562.
1087 Rickard D. and Luther G. W. III (2006) Metal Sulfide Complexes and Clusters. *Reviews in*
1088 *Mineralogy and Geochemistry* **61**, 421–504.
1089 Rickard D. T. (1975) Kinetics and mechanism of pyrite formation at low temperatures.
1090 *American Journal of Science* **275**, 636–652.
1091 Rouxel O. J., Bekker A. and Edwards K. J. (2005) Iron Isotope Constraints on the Archean
1092 and Paleoproterozoic Ocean Redox State. *Science* **307**, 1088–1091.
1093 Savage K. S., Tingle T. N., O'Day P. A., Waychunas G. A. and Bird D. K. (2000) Arsenic
1094 speciation in pyrite and secondary weathering phases, Mother Lode Gold District,
1095 Tuolumne County, California. *Applied Geochemistry* **15**, 1219–1244.
1096 Schmid-Beurmann P. and Bente K. (1995) Stability properties of the CuS2-FeS2 solid
1097 solution series of pyrite type. *Mineralogy and Petrology* **53**, 333–341.
1098 Scholz F. and Neumann T. (2007) Trace element diagenesis in pyrite-rich sediments of the
1099 Achterwasser lagoon, SW Baltic Sea. *Marine Chemistry* **107**, 516–532.
1100 Shea D. and Helz G. R. (1989) Solubility product constants of covellite and a poorly
1101 crystalline copper sulfide precipitate at 298 K. *Geochimica et Cosmochimica Acta* **53**,
1102 229–236.
1103 Shea D. and Helz G. R. (1988) The solubility of copper in sulfidic waters: Sulfide and
1104 polysulfide complexes in equilibrium with covellite. *Geochimica et Cosmochimica*
1105 *Acta* **52**, 1815–1825.
1106 Shikazono N., Nakata M. and Tokuyama E. (1994) Pyrite with high Mn content from the
1107 Nankai Trough formed from subduction-induced cold seepage. *Marine Geology* **118**,
1108 303–313.
1109 Sugawara K., Okabe S. and Tanaka M. (1961) Geochemistry of molybdenum in natural
1110 waters (2). *Journal of Earth Sciences, Nagoya Univ.; (Japan)* **9:1**.
1111 Swanner E. D., Planavsky N. J., Lalonde S. V., Robbins L. J., Bekker A., Rouxel O. J., Saito
1112 M. A., Kappler A., Mojzsis S. J. and Konhauser K. O. (2014) Cobalt and marine redox
1113 evolution. *Earth and Planetary Science Letters* **390**, 253–263.
1114 Swanner E. D., Webb S. M. and Kappler A. (2019) Fate of cobalt and nickel in mackinawite
1115 during diagenetic pyrite formation. *American Mineralogist* **104**, 917–928.
1116 Tauson V.L., Smagunov N.V., Lipko S.V. (2017) Cocrystallization coefficients of Cr, V and
1117 Fe in hydrothermal ore systems (from experimental data). *Russian Geology and*
1118 *Geophysics* **58**, 949-955.
1119 Thomas H. V., Large R. R., Bull S. W., Maslennikov V., Berry R. F., Fraser R., Froud S. and
1120 Moye R. (2011) Pyrite and Pyrrhotite Textures and Composition in Sediments,
1121 Laminated Quartz Veins, and Reefs at Bendigo Gold Mine, Australia: Insights for Ore
1122 Genesis. *Economic Geology* **106**, 1–31.
1123 Tribovillard N., Algeo T. J., Lyons T. and Riboulleau A. (2006) Trace metals as paleoredox
1124 and paleoproductivity proxies: An update. *Chemical Geology* **232**, 12–32.
1125 Tribovillard N., Riboulleau A., Lyons T. and Baudin F. (2004) Enhanced trapping of
1126 molybdenum by sulfurized marine organic matter of marine origin in Mesozoic
1127 limestones and shales. *Chemical Geology* **213**, 385–401.
1128 Vessey C. J. and Lindsay M. B. J. (2020) Aqueous Vanadate Removal by Iron(II)-Bearing
1129 Phases under Anoxic Conditions. *Environmental Science and Technology* **54**, 4006–
1130 4015.
1131 Vorlicek T. P., Helz G. R., Chappaz A., Vue P., Vezina A. and Hunter W. (2018)
1132 Molybdenum Burial Mechanism in Sulfidic Sediments: Iron-Sulfide Pathway. *ACS*
1133 *Earth and Space Chemistry* **2**, 565–576.

Vorlicek T. P., Kahn M. D., Kasuya Y. and Helz G. R. (2004) Capture of molybdenum in pyrite-forming sediments: role of ligand-induced reduction by polysulfides. *Geochimica et Cosmochimica Acta* **68**, 547–556.

Wacey D., Kilburn M. R., Saunders M., Cliff J. and Brasier M. D. (2011) Microfossils of sulphur-metabolizing cells in 3.4-billion-year-old rocks of Western Australia. *Nature Geoscience* **4**, 698–702.

Wagner M., Chappaz A. and Lyons T. W. (2017) Molybdenum speciation and burial pathway in weakly sulfidic environments: Insights from XAFS. *Geochimica et Cosmochimica Acta* **206**, 18–29.

Wang Q. and Morse J. W. (1996) Pyrite formation under conditions approximating those in anoxic sediments I. Pathway and morphology. *Marine Chemistry* **52**, 99–121.

Wang X., Shi M., Zhang J., Pang Y., Zhao Y. (2021) Significance of Trace Elements in Marine Shale Pyrite for Reconstructing the Sedimentary Environment: A Case Study of Niutitang and Hongshuizhuang Formations. *ACS Earth and Space Chemistry* **5**, 3210-3225.

Wei D. and Osseo-Asare K. (1997) Aqueous synthesis of finely divided pyrite particles. *Colloids and Surfaces A: Physicochemical and Engineering Aspects* **121**, 27–36.

Wilkin R. T. and Barnes H. L. (1997) Formation processes of framboidal pyrite. *Geochimica et Cosmochimica Acta* **61**, 323–339.

Wilkin R. T. and Barnes H. L. (1996) Pyrite formation by reactions of iron monosulfides with dissolved inorganic and organic sulfur species. *Geochimica et Cosmochimica Acta* **60**, 4167–4179.

Wilkin R. T., Wallschläger D. and Ford R. G. (2003) Speciation of arsenic in sulfidic waters. *Geochemical Transactions* **4**, 1–7.

Wolthers M., Butler I. B. and Rickard D. (2007) Influence of arsenic on iron sulfide transformations. *Chemical Geology* **236**, 217–227.

Wolthers M., Gaast S. J. V. der and Rickard D. (2003) The structure of disordered mackinawite. *American Mineralogist* **88**, 2007–2015.

Wu M., Xiong Y., JIang N., Ning M., Chen Q. (2004) Hydrothermal preparation of α-MnSe and $MnSe_2$ nanorods. *Journal of Crystal Growth* **262**, 567-571

Zavašnik J., Stanković N., Arshad S. M. and Rečnik A. (2014) Sonochemical synthesis of mackinawite and the role of Cu addition on phase transformations in the Fe–S system. *Journal of Nanoparticule Research* **16**, 2223.

Zhang J., Ren D., Zheng C., Zeng R., Chou C.-L. and Liu J. (2002) Trace element abundances in major minerals of Late Permian coals from southwestern Guizhou province, China. *International Journal of Coal Geology* **53**, 55–64.

Zhu L., Richardson B. J. and Yu Q. (2015) Anisotropic Growth of Iron Pyrite FeS2 Nanocrystals via Oriented Attachment. *Chemistry of Materials* **27**, 3516–3525.